NLR TR 75029 C

ESA CR(P)- 724

NATIONAAL LUCHT- EN RUIMTEVAARTLABORATORIUM

NATIONAL AEROSPACE LABORATORY NLR

THE NETHERLANDS

NLR TR 75029 C

RESTRICTED

PARAMETER ESTIMATION IN MATHEMATICAL MODELS OF THE ESRO 1A ATTITUDE DYNAMICS USING NUMERICAL DIFFERENTIATION OF MEASURED DATA

BY

J.W. BOERSTOEL, G.H. HUIZING and P.TH.L.M. van WOERKOM

Gerubriceerd:
DIENSTGEHEIM
RESTRICTED
DISTRIBUTION RESTREINTE

EUROPEAN SPACE AGENCY
The work described in this report was done under ESA contract. Responsibility for the contents resides in the author or organisation that prepared it.

NLR

RESTRICTED

Gerubriceerd
DIENSTGEHEIM
RESTRICTED
DISTRIBUTION RESTREINTE
B

EUROPEAN SPACE AGENCY
The work described in this report was done under ESA contract. Responsibility for the contents resides in the author or organisation that prepared it.

NLR TR 75029 C

PARAMETER ESTIMATION IN MATHEMATICAL MODELS OF THE ESRO 1A ATTITUDE DYNAMICS USING NUMERICAL DIFFERENTIATION OF MEASURED DATA

by

J.W. Boerstoel, G.H. Huizing and P.Th.L.M. van Woerkom

SUMMARY

Purpose of the present study is the investigation of the validity of a new algorithm for the estimation of parameters related to spacecraft torques. The algorithm is based on data reduction by numerical differentiation using smoothing splines. Measured data of the ESRO 1A "Aurorae" spacecraft are used.

It is concluded that the new data reduction algorithm is stable and efficient. So-called end effects of the smoothing splines cause minor problems, however. It is further concluded that the mathematical model for the spacecraft torques may be improved; better models are proposed.

The algorithm appears to be a powerful tool for accurate estimation of in-orbit spacecraft torque parameters.

Part of the investigations were performed for the European Space Research Organization under ESOC contract CTR 592/73/AR.

Division: Sc. Serv.
Space Flight Techn.
Prepared: JWB/GHH/PThLMvW/
Approved: WL/PK

Completed : 4-XII-1974
Ordernumbers : 554.402, 201.402
Typ. : CS

CONTENTS

1 Table (in text)
17 Figures

CONTENTS (continued)

LIST OF SYMBOLS

a	vector of parameter a_j in mathematical model for the spacecraft attitude dynamics
a_j	parameter in vector a_j
f(t)	function of time, Eq. (7)
F	fit measure, Eq. (8)
g(t)	function of time minimizing expression (9)
I	inertia dyadic
i	data point count; vector component count
j	parameter count
k	quaternion parameter count
L_{M_1}	torque on satellite due to permanent magnet
L_{M_2}	torque on satellite due to damping rods
L_{M_3}	torque on satellite due to gravity gradient
L_T	inertial torque, Eq. (2)
n	number of data points in a sequence of data points
q	order of derivative, Eq. (7)
S	smoothness measure, Eq. (7)
t	time
t_1	time at first data point of a sequence of data points
t_n	time at last data point of a sequence of data points
t_i	time at i-th data point of a sequence of data points
u	quaternion parameter vector
u_k	k-th component of u
y_i	measurement at i-th data point of a sequence of data points

ω	angular velocity vector (body-fixed co-ordinate system)
ω_i	i-th component of ω
$(\dot{\ })$	first derivative with respect to time
$(\ddot{\ })$	second derivative with respect to time

N.B.: Symbols occurring in appendices are explained in the text of the appendices.

The following three Cartesian co-ordinate systems are used:

- a geocentric, earth-fixed system (fixed with respect to the rotating Earth)
- a geocentric, inertially fixed system (fixed with respect to the stars)
- a spacecraft centered, body-fixed system (fixed with respect to the moving spacecraft).

The precise definition of each of these three co-ordinate systems is not needed in this report. The reader is referred to reference 7 for the many details.

1 INTRODUCTION

In this study the validity of a new algorithm for the estimation of parameters related to spacecraft torques is analyzed. The algorithm is based on reduction of measured data by numerical differentiation using smoothing splines. Measured data of the ESRO 1A "Aurorae" spacecraft are used.

The algorithm was proposed by Fraiture (Ref. 1) and elaborated by Schmidtbauer (Ref. 2).

In general, parameter estimation techniques are time consuming computational processes when during the minimization the differential equations for the attitude motion have to be repeatedly integrated numerically. In principle it is possible, however, to replace the numerical integrations by numerical differentiations of measured data, and to use the differential equations (containing the parameters) as they stand to obtain a best fit between measurements and mathematical model. This approach may be expected to be potentially more economical.

Stable and efficient algorithms for numerical differentiation have been developed in recent years. The present study investigates the potential of such differentiation algorithms using ESRO 1A spacecraft data as input. It is found that such algorithms may be efficient numerical tools in parameter estimation studies.

2 MEASUREMENTS

The ESRO-IA spacecraft was launched on 4 October 1968 into a near-earth polar orbit (perigee 259 km, apogee 1535 km). It had passive magnetic stabilization with two strong ferromagnets aligning the spacecrafts z-axis along the earth magnetic field lines. The z-axis oscillated around these lines with a period of 6 to 12 minutes. The oscillations were damped by a set of highly permeable magnetic rods (hysteresis damping).

The direction to the sun in a spacecraft-fixed co-ordinate system was measured with five digital two-slit solar sensors covering all possible view angles. The direction and magnitude of the earth magnetic field vector were measured with four magneto meters covering angles of at least 22° between the spacecraft's z-axis and the earth magnetic field lines. The directions of these two vectors were measured with a total error of at most ± 0.5° (solar sensors) and ± 1.5° (magneto meters).

The measured solar angles and magnetic field vectors were sampled every 6.4 seconds, transmitted to the ground and recorded on so-called Archive tapes, together with information about the spacecraft position and the time of sampling.

The measurements are grouped in so-called apogee passes. Each pass comprises 300 to 600 measurements covering one third to two thirds of a complete orbit of the satellite (orbit period about 100 minutes).

A discussion of the selection of passes in this study is presented in appendix A. Twenty two passes out of a sample of 130 passes were found to satisfy the quality criteria of the measured data and are available for use in computations.

3 FORMULATION OF VALIDITY TEST

The preliminary study of Schmidtbauer (Ref. 2) permitted the conclusion that it is possible to estimate parameters that occur in the equations describing the attitude motion of the ESRO IA spacecraft.

In order to realize this a mathematical model for the spacecraft attitude motion, a smoothing differentiation algorithm and a parameter estimation technique (for parameters in the mathematical model) have to be combined in one algorithm. The concepts of this algorithm are presented in sections 3.1 through 3.4. Section 3.5 contains a description of an algorithm for checking the results of parameter estimation by integration. A summary of the validation test is given in section 3.6.

3.1 Mathematical model for spacecraft motion

The attitude behaviour of the spacecraft is analyzed with the Euler vector equation (in a body-fixed co-ordinate system):

$$L_T = I.\dot{\omega} + \omega \times (I.\omega) = \text{inertial torque} \tag{1}$$

where $L_{M_1} + L_{M_2} + L_{M_3} = L_T$; (2)

L_{M_1} = torque on the satellite due to the permanent magnets;
L_{M_2} = torque on the satellite due to the damping rods;
L_{M_3} = gravity gradient torque;
I = spacecrafts inertia dyadic;
ω = angular velocity vector,

and where the dot denotes differentiation with respect to time. The equation relates angular velocities and accelerations to the torques exerted on the spacecraft. In order to be able to disregard aerodynamic effects only orbit parts at altitudes above 700 km have been considered (Appendix G2).

Models for the inertia dyadic and the exerted torques may be found in reference 2. The vector equation (1) and (2) contain five parameters of which the magnitude is not accurately known. These parameters have to be estimated. The parameters occur in the functional forms:

$$I = I(a_2) \tag{3}$$

$$L_{M_1} = L_{M_1}(a_1, a_3, a_4) \tag{4}$$

$$L_{M_2} = L_{M_2}\,(a_5) \qquad (5)$$

$$L_{M_3} = L_{M_3}\,(I(a_2)) \qquad (6)$$

The precise form of the equations is given in reference 2, equations (4.2), (4.5), (4.22) and (4.27).

As the orientation of two of the principal inertia axes is not accurately known, a rotation parameter a_2 is introduced in order to permit the estimation of the orientation. The magnetic dipole moment vector of the permanent magnets is parametrized by a_1 (for magnitude) and a_3, a_4 (allowing for small misalignment with respect to the nominal orientation). The magnitude of the magnetic damping is determined by a parameter a_5. The hysteresis rods also decrease the effective magnitude of the magnetic dipole moment of the permanent magnets; in reference 2 it has been assumed that the parameter a_1 can be used to account for this effect.

3.2 Data processing and numerical differentiation

Input to the parameter optimization are angular velocities and accelerations, earth magnetic field strengths and the spacecraft orientations in a geocentric inertial co-ordinate system. These data are computed from the measurements of a pass using a technique proposed by Fraiture (Ref. 1).

The following measured data are available at the data points of a pass (at time intervals of 6.4 seconds):

- direction to the sun } in body-fixed co-ordinate system;
- earth magnetic field vector } in body-fixed co-ordinate system;
- time (time of day, day, year);
- position (in earth-fixed co-ordinate system).

The last two quantities are used to calculate at each data point:

- a model direction to the sun } in a geocentric inertial co-ordinate system.
- a model earth magnetic field vector } in a geocentric inertial co-ordinate system.

A comparison at each data point between measured and model vector for the sun direction and the earth magnetic field allows the determination of the attitude of the spacecraft in the geocentric inertial co-ordinate system at each data point.

The output of the data processing is a sequence of data points with:

- the measured earth magnetic field vector (in body-fixed co-ordinates);
- the time;
- quaternion parameters u_k, $k = 1(1)4$, specifying the measured spacecraft attitude. 1)

The angular velocities ω and angular accelerations $\dot{\omega}$ at the data points are computed from this output by numerically differentiating the quaternion parameters twice with respect to time and applying the transformation (E1) of Appendix E.

The differentiation of the quaternion parameters constitutes a critical part in the entire computation process because the parameters are contaminated with noise due to measurement errors. Smoothing is necessary to cope with this noise.

The numerical differentiation is accomplished with an algorithm using the smoothing spline function theory proposed by Anselone and Laurent (Ref. 4).

1) Quaternion parameters can be used to describe the rotation of a co-ordinate system to a new orientation. For details about their theory and use see e.g. references 1 and 3.

In this algorithm a balance is made between a smoothness measure of a function, $f(t)$, defined by:

$$S = \int_{t_1}^{t_n} \left\{ f^{(q)}(t) \right\}^2 dt, \tag{7}$$

($q \geqq 1$ order of the derivative) and a fit measure of that function to a given set of points (t_i, y_i):

$$F = \sum_{i=1}^{n} \left\{ f(t_i) - y_i \right\}^2 \tag{8}$$

Anselone and Laurent prove that the problem of minimizing (for a given fixed value of the parameter ρ) the expression

$$S + \rho F \tag{9}$$

by varying $f(t)$ (within a certain given class of functions) has as a solution a unique function $g(t)$, provided the end conditions

$$g^{(q)} = g^{(q+1)} = \ldots = 0 \text{ at } t=t, \text{ and } t=t_n \tag{10}$$

are satisfied.

Some details of the application of this algorithm are given in appendix B. In the computations q was given the values 2 and 3.

3.3 Parameter estimation

The parameters $a_j, j = 1(1)5$, in the mathematical model for the spacecraft attitude dynamics are estimated by a least squares method based on equations (1) and (2). These equations are satisfied if the Euclidian norm

$$\left\| \left\{ L_{M_1}(a_1,a_2,a_3) + L_{M_2}(a_5) + L_{M_3}(I(a_2)) \right\} - \left\{ I(a_2) \, . \, \dot{\omega} + \right. \right. \\ \left. \left. + \, \omega * (I(a_2) \, . \, \omega) \right\} \right\| \tag{11}$$

of the vector inside the $\| \;\; \|$ signs is zero.

For each pass available the parameters a_j are estimated by minimizing the sum of the squared norms at the data points:

$$E = \sum_{i=1}^{n} \left(\left\| \left\{ L_{M_1} + L_{M_2} + L_{M_3} \right\} - \left\{ I.\dot{\omega} + \omega * (I.\omega) \right\} \right\|_i \right)^2 \qquad (12)$$

$i = 1(1)n$: data point count

This expression turns out to be non-quadratic in the parameters a_j.

From the results of reference 2 it is clear that the minimum is poorly defined. It was therefore decided to replace the minimization algorithm of reference 2 by that of Fletcher (Ref. 5), and to solve the systems of linear equations in Fletcher's iteration technique by methods that are capable to recognize and handle ill-conditioned and singular systems of linear equations (Ref. 6). Details of the minimization technique are given in appendix C.

3.4 The program system for parameter estimation

For the purpose of the parameter estimation a system of five computer programs was developed and used. Two programs are used for data collection from Archive tapes and for further data manipulation. Three separate programs are used for numerical differentiation, parameter optimization and plotting of numerically differentiated data.

The programs accept as input the measured data of a pass and a few parameters needed for control of the computations. The output consists of:

- estimates of the parameters a_j;
- residual torque $(L_{M_1} + L_{M_2} + L_{M_3} - L_T)$ and torques $L_{M_1} + L_{M_2}$, L_{M_3} and L_T (component-wise for each data point);

- statistics of the residual torque (variance);
- the raw and smoothed quaternion parameters u_k and their first two derivatives together with statistics of the differences between raw and smoothed data (component-wise for each data point);
- the angular velocities ω and accelerations $\dot{\omega}$ (component-wise for each data point).

A systems flow chart is discussed in appendix D.

3.5 Integration algorithm

The validity of the estimated parameter values was checked in a few cases by integrating the dynamical equations of the spacecraft attitude motion, equation (1), and comparing the measured attitude during a pass (or a segment of a pass) with that obtained by numerical integration. During integration the parameters a_j in the mathematical model were given their estimated values. Integrations were performed forward or backward in time starting at a suitable data point of the measured pass.

A norm on the angular difference between measured and computed attitude was chosen as error measure (equation (E2)).
It may be expected that the numerical value of this norm increases from zero during the integration process.

Details of the algorithm are presented in appendix E.

3.6 Summary of validation test

In order to test the validity of the mathematical model and of the numerical differentiation algorithm the program system for parameter estimation is used with the measured data of each of the 22 available passes as input. The results are 22 estimates of the parameters a_j and statistics (averages, variances, rms values) of residual torques, residual quaternion parameters, etc. A second step in the validation test is an attempt to answer the question whether the results are acceptable from an engineering point of view.

Some results are checked with the integration algorithm (one pass).

Results of the validation test are presented in section 4 and discussed in section 5.

4 VALIDATION TEST RESULTS

The results of the running of the program system for parameter estimation are presented in table 1. The average values of the parameters over all passes and their a priori estimates are given at the lower end of the table.

Table 1 : Parameter estimates and rms-values of residual torques of 22 passes.

Pass no	No of data points	1st data point	Parameter estimates					Residual torques			
			a_1 A.M.^{2}	a_2 RADIANS	a_3 –	a_4 –	$a_5 \cdot 10^{-8}$ A.M^4 sec/V	RMS tot. DYNE CM	RMS x DYNE CM	RMS y DYNE CM	RMS z DYNE CM
2039	364	1	24.28	.4985	.007142	.01874	+ 3.91	50	54	61	29
2919	360	104	24.48	.4165	.004885	.01658	– 3.17	55	63	70	13
1912	400	1	24.51	.4231	.004773	.01522	– 2.31	51	51	64	33
1913	350	1	23.99	.3353	.004452	.01282	+ 2.05	61	57	84	26
1921	400	283	25.57	.4472	.007307	.02375	– 83.55	48	56	48	40
1928	358	1	25.82	.3677	.007359	.02121	+ 1.13	51	62	51	39
1933	400	200	23.60	.4220	.003902	.01522	+ 4,62	139	198	115	70
1915	400	302	25.15	.4553	.005499	.01590	+ 0.54	45	59	47	16
1905	400	350	25.16	.3958	.008918	.01786	+ 30.70	54	74	50	28
2471	380	1	23.56	.0797	.000993	.00777	– 32.79	90	142	56	29
2123	270	1	23.42	.0112	.003285	.01154	+ 1.66	45	62	45	16
2129	400	1	24.62	.3527	.006570	.01250	– 5.74	31	41	29	18
2148	400	233	23.87	.3932	+.010751	.01175	+ 21.94	92	55	145	32
2153	374	368	23.92	.4745	–.009026	.02781	+ 23.29	92	115	106	32
2154	314	352	23.94	.4706	+.002536	.02358	+ 17.36	139	158	176	42
2155	364	325	24.71	.3475	+.001713	.02252	+ 40.72	117	160	114	52
2170	400	304	24.80	.4415	.002906	.01287	+ 5.17	96	85	136	41
2175	400	275	24.17	.1399	.001316	.01167	+ 8.46	58	43	88	23
2113	358	325	24.29	.1889	.004013	.01124	+ 38.47	90	118	97	31
2118	400	300	24.47	.1664	.004122	.01347	+ 0.43	56	80	45	29
2108	400	1	24.61	.4760	.005374	.01339	– 3.13	68	64	95	25
2456	400	1	25.30	.1709	.005071	.02765	+ 9.16	122	145	140	66
Average and a priori values of the parameters											
Averages			24.47	.34	.004	.016		75	88	85	33
A priori values (from Ref. 7 and App. G)			~24	.35	0	0	+ 5				

The relevance of these numerical results can only be appreciated if additional results of the application of the algorithm for the parameters estimation are analyzed. This will be done mainly in section 5. A few results are:

- The angular differences between model and measured sun directions and earth magnetic field lines are of the order of one degree.
- The differences between model and measured magnitudes of the earth magnetic field are of the order of one percent of the average magnitude.
- The maximum values of the differences between raw and smoothed quaternion parameters (computed during numerical differentiation) are of the order of one percent.
- The accuracy of the numerical computation of the estimates of the parameters a_j for each pass separately is at least:

	a_1	.0001
	a_2	.00001
	a_3	.00001
	a_4	.00001
10^{-8}	a_5	.01

  (These numbers are deduced from differences between values of the parameters at the last few iteration steps in the minimization technique). As these numbers are considerably smaller than the dispersion of the estimates in table 1, it may be concluded that the estimates are not contaminated with numerical errors due to ill-conditioness of the minimization problem or to imperfect tuning of the tolerance tests terminating the minimizing iteration.
- The programs were thoroughly tested for correctness (in particular the smoothing differentiation and minimization programs) by applying them to model problems.

Results obtained with the application of the numerical integration program are presented in the next section and in appendix H.

5 DISCUSSION OF TEST RESULTS

The results presented in table 1 are disappointing in several respects. Taking into account that the accuracy of the raw quaternion parameters is of the order of one percent and that 300 to 400 data points are available to estimate the five parameters a_j, one would expect that:

a. the differences between the parameters and their overall averages would be only a few percent of the average values;

b. the residual torques would be about one percent of the order of magnitude of the total torque. As the total torque is of the order of 1000 dyne cm, the residual torques should be 10 to 20 dyne cm. The actual values are about 75 dyne cm.

The disappointing results are due to imperfections in the mathematical model for the torques and for imperfections in the data processing and numerical smoothing algorithms. An effort has been made to clarify the situation; the results are discussed in the remainder of this section.

A list of possible causes for the problem was first compiled:

- effect of sun sensor switching;
- modelling of the inertia dyadic (partially deployed booms);
- aerodynamic torque effects;
- solar radiation torque effects;
- modelling of the permanent magnets and magnetic damping system;
- imperfections in the data processing loop;
- imperfections in the numerical differentiation algorithm.

The points on this list will be discussed separately in the next sections.

The residual torques shown in table 1 are smaller than those presented in reference 2. This is due to improvements made in the algorithm.

5.1 Sun sensor switching

The measured values of the direction vector to the sun are obtained at each data point from one of the five solar sensors. When sun sensor switching occurs between two successive data points, additional errors may be generated.

Using data of pass 2129 it was found that these additional errors are of the order of 0.2° or less. This value is considerably less than the overall accuracy of 1° of the measurements.

It is thus evident that sun sensor switching does not introduce significant errors.

5.2 Modelling of the inertia dyadic

In reference 7 the possibility of partial boom deployment is mentioned. If one or more of the booms are only partially deployed the inertia dyadic will not have the form assumed in reference 2.

Some parameter estimates were made with the inertia dyadic completely parametrized with the exception of one diagonal element (the element $I_{33} = 5.53$ kgm^2 (see equations (4.4) and (4.5) of Ref. 2), as that element is accurately known.

The estimated values turned out to differ too much from the a priori values. This was probably due to other disturbing effects to be discussed below. Incorrect modelling of the inertia dyadic, although unlikely, must still be considered a possibility, however, because the numerical testing was not exhaustive.

5.3 Aerodynamic torque effects

All data points were taken at altitudes above 700 km. At these altitudes the aerodynamic torque should be at most of the order of the expected residual torque level. If the aerodynamic torque is larger it would not be permitted to neglect it.

In appendix G2 an estimate is made of the maximum of the aerodynamic torque on the spacecraft. This maximum is found to be of the order of 2 dyne cm at altitude of 700 km (Eq. (G10)).

Aerodynamic torques are thus not responsible for the high error level.

5.4 Solar radiation torque effects

In appendix G3 it is estimated that the torque on the spacecraft due to solar radiation is of the order of one dyne cm at most. Solar radiation effects are thus not significant.

5.5 Modelling of the permanent magnets and the magnetic damping system

From the fact that the estimates of the parameters a_1, a_3, a_4 and a_5 (occurring in the mathematical model for the permanent magnets and the magnetic hysteresis rods) show rather large dispersion it can be concluded that the magnetic modelling is probably incorrect.

The modelling of the permanent magnet and magnetic damping system is investigated in appendix F. It is concluded that the modelling of both the effective permanent magnet and the hysteresis rods is probably incorrect. The incorrectness is already sufficient to account completely for the dispersion of the a_1, a_3, a_4 and a_5 parameters.

Specifically, the errors concern the modelling of the magnetic damping system(hysteresis rods). In reference 2 it is assumed that the rods are parallel to the spacecraft x- and y-axes; in reality they are oriented along the bisectrices of the angles between the x- and y-axes. As a consequence the damping torques (order of magnitude 20 dyne cm, see appendix G4, equation (G26)) cannot be correctly estimated. Furthermore, it is shown in appendix F that the decrease of the effective magnitude of the permanent magnets by the hysteresis rods is a dynamic effect. In appendix G4 the magnitude of this dynamic effect is estimated to be of the order of ten percent of the magnetic dipole moment of the permanent magnets (26.6 Am^2). In reference 2 this dynamic effect is not taken into account.

The analysis of the modelling of the magnetic damping system is based on the assumption that the magnetic effects of the rods can be adequately based on the application of the Rayleigh model for the relation between external magnetic field and induced magnetic induction. There appears to be no reason to distrust the applicability of the Rayleigh model.

5.6 Imperfections in the data processing loop

There are at least two related points concerning the data processing that are worth to be considered:

- the normalization of the quaternion parameters;
- the computation of angular velocities and accelerations from quaternion parameters.

The quaternion parameters satisfy the normalizing relation (Refs. 1 and 3)

$$\sum_{k=1}^{4} u_k^2 = 1$$

The first and second derivatives of the parameters with respect to time should thus satisfy the relations:

$$\sum_{k=1}^{4} u_k \dot{u}_k = 0$$

$$\sum_{k=1}^{4} (u_k \ddot{u}_k + \dot{u}_k^2) = 0$$

The first and second derivatives of the smoothed quaternion parameters were not corrected to account for the last two relations.

The computation of the angular velocities ω from the smoothed quaternion parameters occurs with a system of four equations for three unknowns (equation (E1) in appendix E). As long as equations (12) and (13) are satisfied this system has a unique solution, otherwise, it is usually overdetermined. In the present parameter estimation algorithm an ESOC subroutine was used, that selects from the four equations three equations that may be expected to be well-conditioned. However, this will introduce discontinuities in ω when equations (13) are not precisely satisfied and the subroutine changes its selection of equations. The same conclusion may be drawn for $\dot{\omega}$. The discontinuities in ω and $\dot{\omega}$ occasionally introduce jumps in the residual torques of over 60 dyne cm.

5.7 Imperfections in the numerical differentiation algorithm

In appendix H an analysis is presented of the numerical performance of the smoothing spline function algorithm and the results obtained with the numerical integration algorithm.

The conclusion is that so-called end effects of the spline functions introduce large errors, that are not present in the measured data. The end effects are due to the end conditions (10); these are physically incorrect as the second derivatives of the quaternion parameters actually resemble periodic functions. The end effects may account for residual torques of over 100 dyne cm in roughly the first and last 50 data points of a pass.

The presence of end-effects is also evident from experiences with numerical integration: the maximum of the norm ϑ of the error angle (appendix E, equation (E2)) was reduced from 32° (over 400 data points) to about 12° (over 320 data points) by excluding the first 60 data points of a pass.

The smoothing spline function algorithm can possibly be improved either by making a physically more relevant assumption about the end conditions or by introducing better smoothness measures than the one defined by equation (7). The end conditions (10) may be replaced by

$$g^{(0)},\ g^{(1)},\ g^{(q-1)} \text{ prescribed at } t=t_1 \text{ and } t=t_n \tag{14}$$

without much change in the algorithms. The smoothness measure (7) could perhaps be replaced by a measure of the form

$$S = \int_{t_1}^{t_n} \left\{ f^{(q)} - c(t) \right\}^2 dt \tag{15}$$

where c(t) is a function of t estimated such that it is a better estimate of the q-th derivative of the quaternion parameters than the function identically zero. The algorithms have to be rather drastically changed in this case.

The numerical stability and efficiency of the smoothing spline function algorithms proposed by Anselone and Laurent (Ref. 4) was found to be noteworthy.

6 AERODYNAMIC TORQUES OVER PERIGEE PASSES

The aerodynamic torques exerted on the spacecraft at low altitudes may be sufficiently large to permit a quantitative analysis of these effects.

If models for the aerodynamic interaction between spacecraft and atmosphere contain parameters that are not accurately known, these may be estimated. In order to obtain sufficiently accurate estimates the aerodynamic torques should on the average be large compared to the residual torques.

In appendix I it is estimated, that the aerodynamic torques vary from about 12.8 dyne cm at 500 km altitude to about 573.6 dyne cm at perigee (260 km altitude), and that about 34.08 minutes, equivalent to 330 data points, are available if a pass contains a trajectory from 500 km altitude down to perigee and up again to 500 km.

It may be concluded that the aerodynamic torques and the number of data points are sufficiently large to permit the estimation of parameters in aerodynamic interaction models. In particular, if the residual torque level of the present parameter estimation algorithm could be reduced to 10 to 20 dyne cm (this seems to be feasible by improving the modelling of the effects of the magnetic damping-system and excluding the begin and end of smoothed data sequences), relevant aerodynamic parameters can be estimated with a precision of seven percent (average signal to noise ratio: $1/2 * 573.6 : 20 \Longrightarrow$ signal to noise ratio in parameters : 14 : 1).

7 CONCLUSIONS

The main conclusions of the validation test of the parameter estimation algorithm proposed in reference 1 and subjected to a preliminary investigation in reference 2, are:

- The smoothing spline function algorithms proposed by Anselone and Laurent (Ref. 4) are very stable and efficient from a computational point of view.
- The application of the smoothing spline function algorithm to the sequences of data occurring in this study introduces so-called end effects. These are due to the fact that the modelling of the data in the theory for the smoothing spline functions is physically incorrect at the end points.
- The modelling of damping effects of the highly permeable magnetic rods is incorrect.
- The minimization algorithm applied in this study does not contri-

bute to uncertainties and errors.

- It seems possible to estimate relevant parameters in models for the aerodynamic interaction with an accuracy of, say, ten percent.
- It is expected that the residual torques can be reduced significantly by correcting the various shortcomings.

8 REFERENCES

1	Fraiture, L.	Working paper on the torque determination from known attitude for ESRO I A/B. ESOC(ESRO), Darmstadt, February 1970.
2	Schmidtbauer, B.	Determination of realistic disturbance torque parameters using ESRO 1A data. SAAB-SCANIA Report RA-SAT - 3.4 - C - 006, December 1972.
3	Whittaker, E.T.	A treatise on the analytical dynamics of particles and rigid bodies, Chapter 1, Cambr. Univ. Press, 4th Ed., 1965.
4	Anselone, P.M. and Laurent, P.J.	A general method for the construction of interpolating or smoothing spline functions. Num. Math. 12, pp. 66-82, 1968.
5	Fletcher, R.	Generalized inverse methods for the best least squares solution of systems of non-linear equations, Comp. J., 10, pp. 392-399, 1968
6	Hanson, R.J. and Lawson, C.L.	Extensions and applications of the Householder algorithm for solving linear least squares problems, Math. Comp., 23, no 108, pp. 787-812, 1969.

7 Fraiture, L. Technical information file on ESRO IA - Addendum to the call for tender TA/58/71/AR. ESOC(ESRO), Darmstadt.

8 Daily solar data and orbital data for the period 1 October 1968 to 1 May 1969, supplied by ESOC. See also: K.G. Lenhart, "Geomagnetic and solar data for use with digital computers". Transactions American Geophysical Union, Vol. 49, No. 2, June 1968, pp. 463-464.

9 Kip, A.F. Fundamentals of electricity and magnetism. McGraw-Hill Book Company, N.Y., 1962.

10 Spacecraft magnetic torques. NASA SP-8018, March 1969.

11 Fischell, R.E. "Magnetic and gravity attitude stabilization of earth satellites". In: COSPAR Space Research II, H.C. van de Hulst et al., eds., North-Holland Publishing Company, Amsterdam, 1961, pp. 373-410.

12 Fröhlich, H., Mesch, F., Schweizer, G. and Stopfkuchen, K. Passiv magnetische Lageregelung von Erdsatelliten. Bundesministerium für Bildung and Wissenschaft, Forschungsbericht W70-05, Februar 1970.

13 Mesch, F. Schweizer, G. and Stopfkuchen, K. "Investigation of earth satellites with magnetic attitude stabilization". In: Peaceful Uses of Automation in Outer Space, J.A. Aseltine, ed., Plenum Press, N.Y., 1966, pp. 176-210

14 Abraham, M. and Becker, R. — The classical theory of electricity and magnetism. Second edition, Blackie and Son Limited, London, 1961.

15 ESRO-I Spacecraft Description Document. ESRO Technical Report TR-10 (ESTEC), May 1972.

16 The ESRO satellite "Aurorae" interim report on behaviour in orbit. ESRO TN-92 (ESTEC), March 1969.

17 Nelson, W.C. and Loft, E.E. — Space Mechanics. Prentice-Hall Inc., Englewood Cliffs, N.J., 1962, pp. 160-163.

18 Van Woerkom, P.Th.L.M. — Generalized models for the study of interaction between spacecraft and atmosphere. Preprint 74-063, XXV-th International Astronautical Congress, Amsterdam, 30 September - 5 October 1974.

19 Marov, M.Ya. and Alpherov, A.M. — "Semi-annual density variations of the atmosphere at heights of 200-300 km". COSPAR Space Research XII, Volume 1, Akademie-Verlag, Berlin, 1972, pp. 803-808.

20 Committee on space research. — Cospar International Reference Atmosphere CIRA 1965. North-Holland Publishing Company, Amsterdam, 1965.

21 Evans, W.J. — "Aerodynamic and radiation disturbance torques on satellites having complex geometry". In: Torques and Attitude Sensing in Earth Satellites, S.F. Singer, ed., Academic Press, N.Y. 1964, pp. 83-98.

22 Spacecraft Radiation Torques.
NASA SP-8027, October 1969.

23 Boerstoel, J.W. and Van Woerkom, P.Th.L.M. Response to ESOC call for competitive offers reference TA/105/73/AR for an "Applied research study on torque analysis and parameter estimation".
NLR, 5 November 1973.

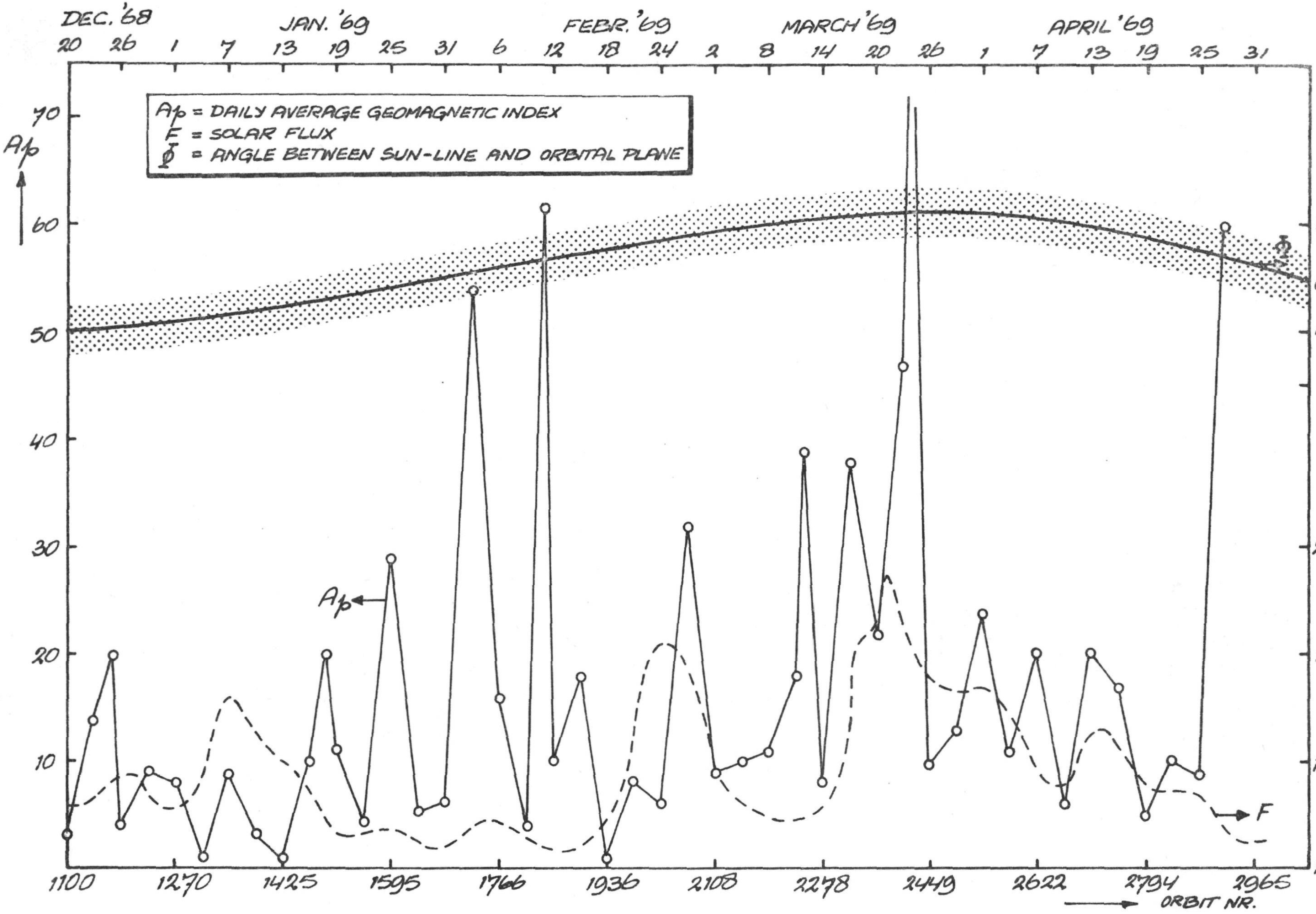

Fig.1 Data used for selection of passes

See appendix A

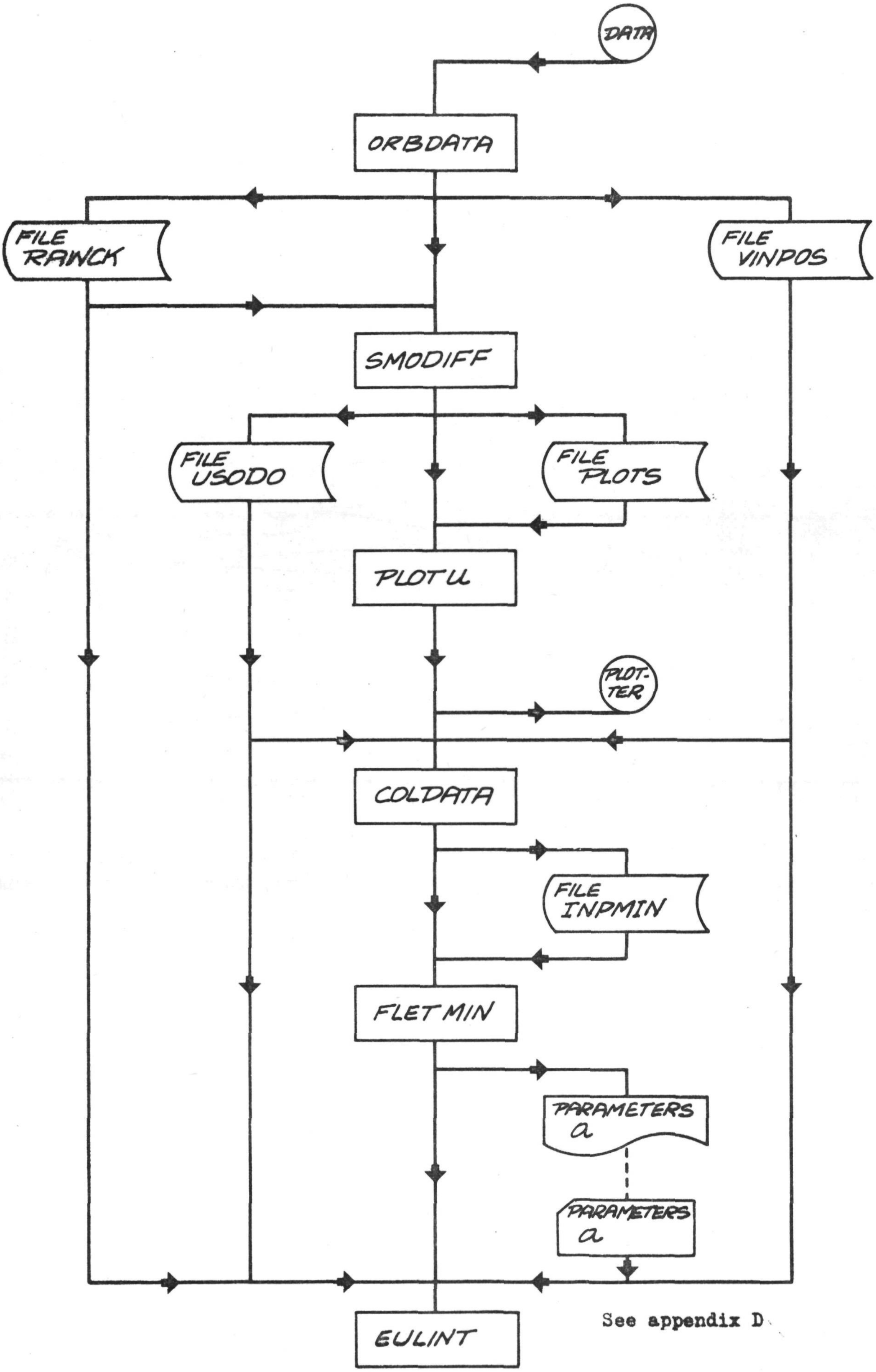

Fig.2 Program and file system

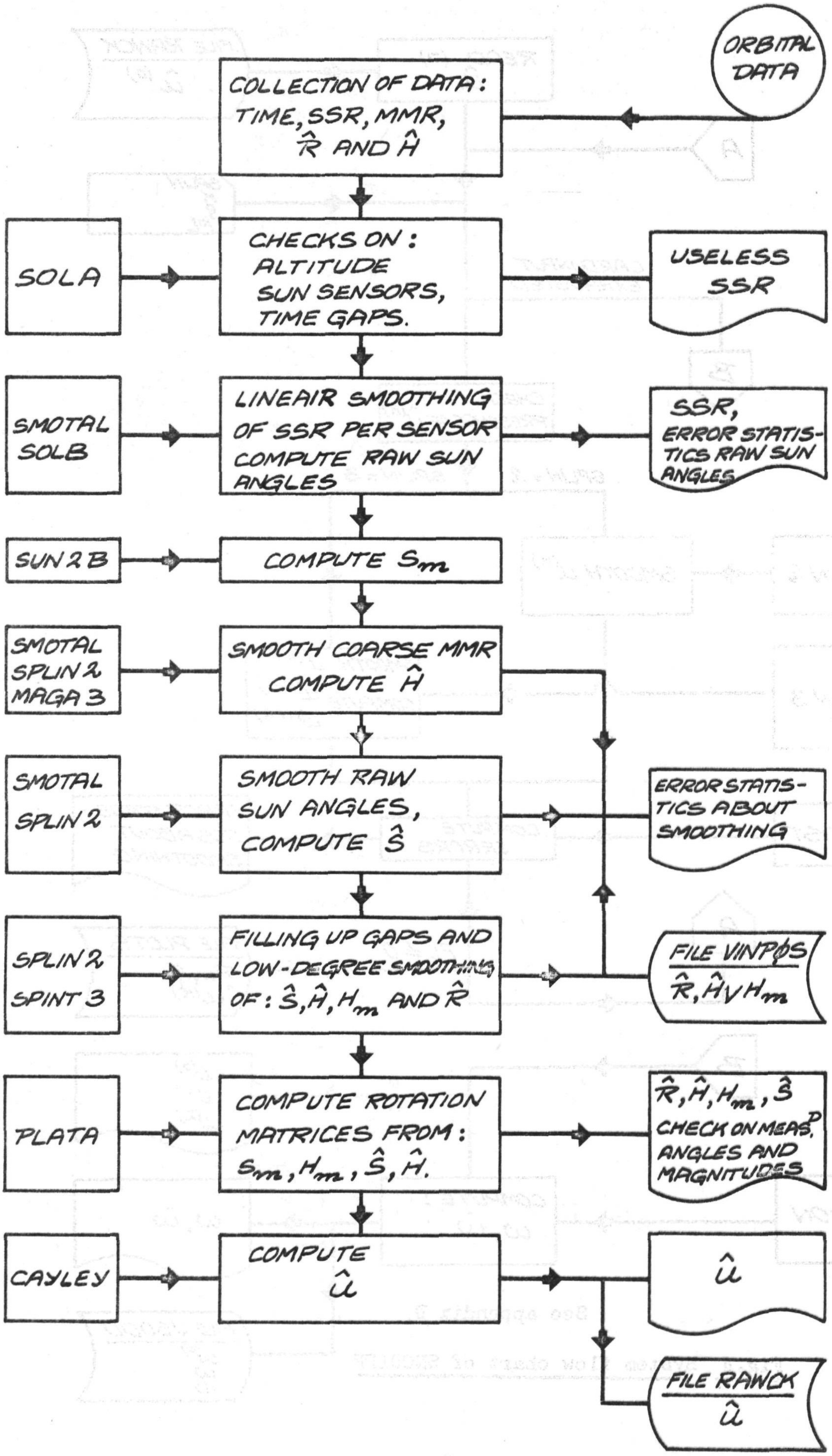

See appendix D

Fig.3 System flow chart of ORBDATA

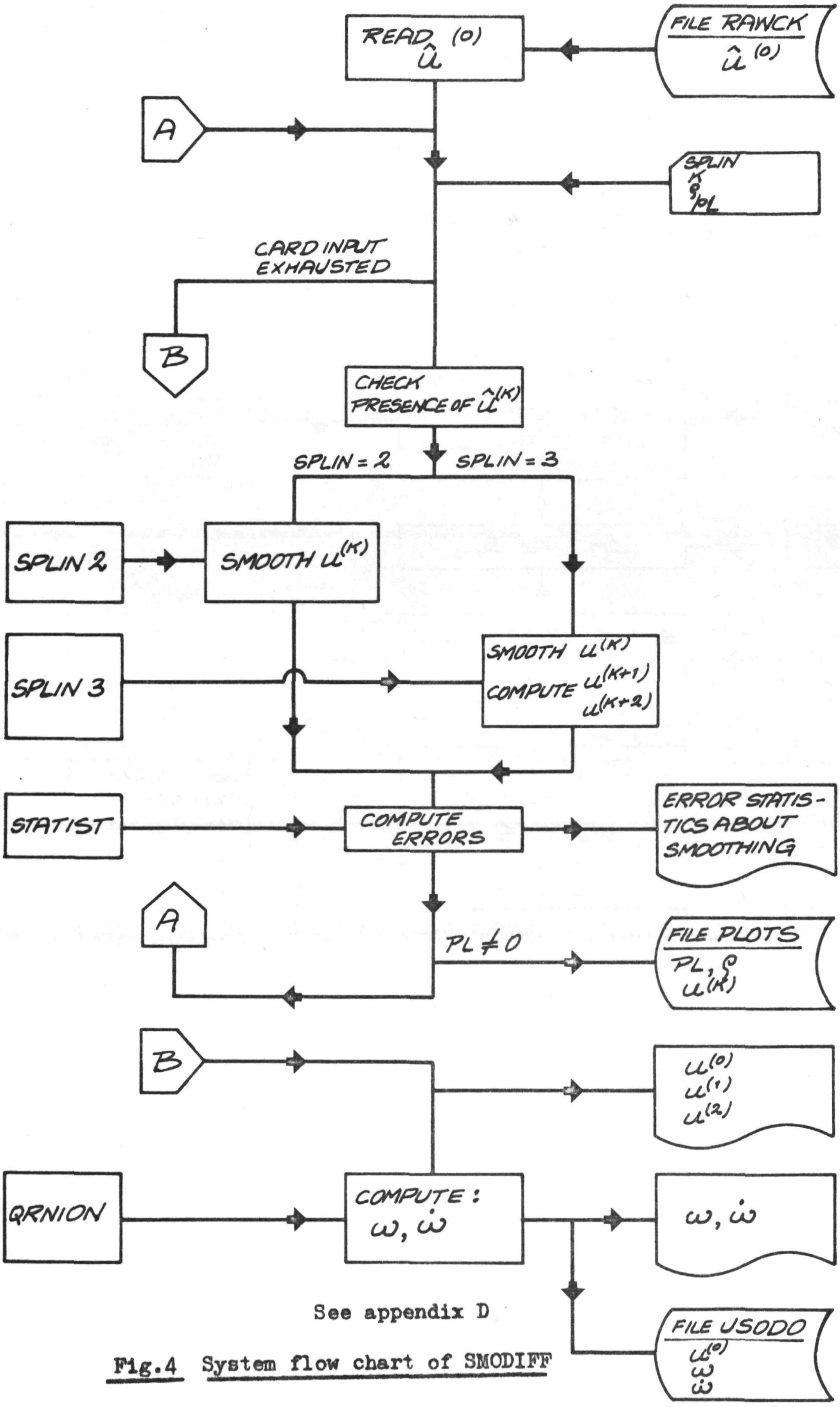

See appendix D

Fig.4 System flow chart of SMODIFF

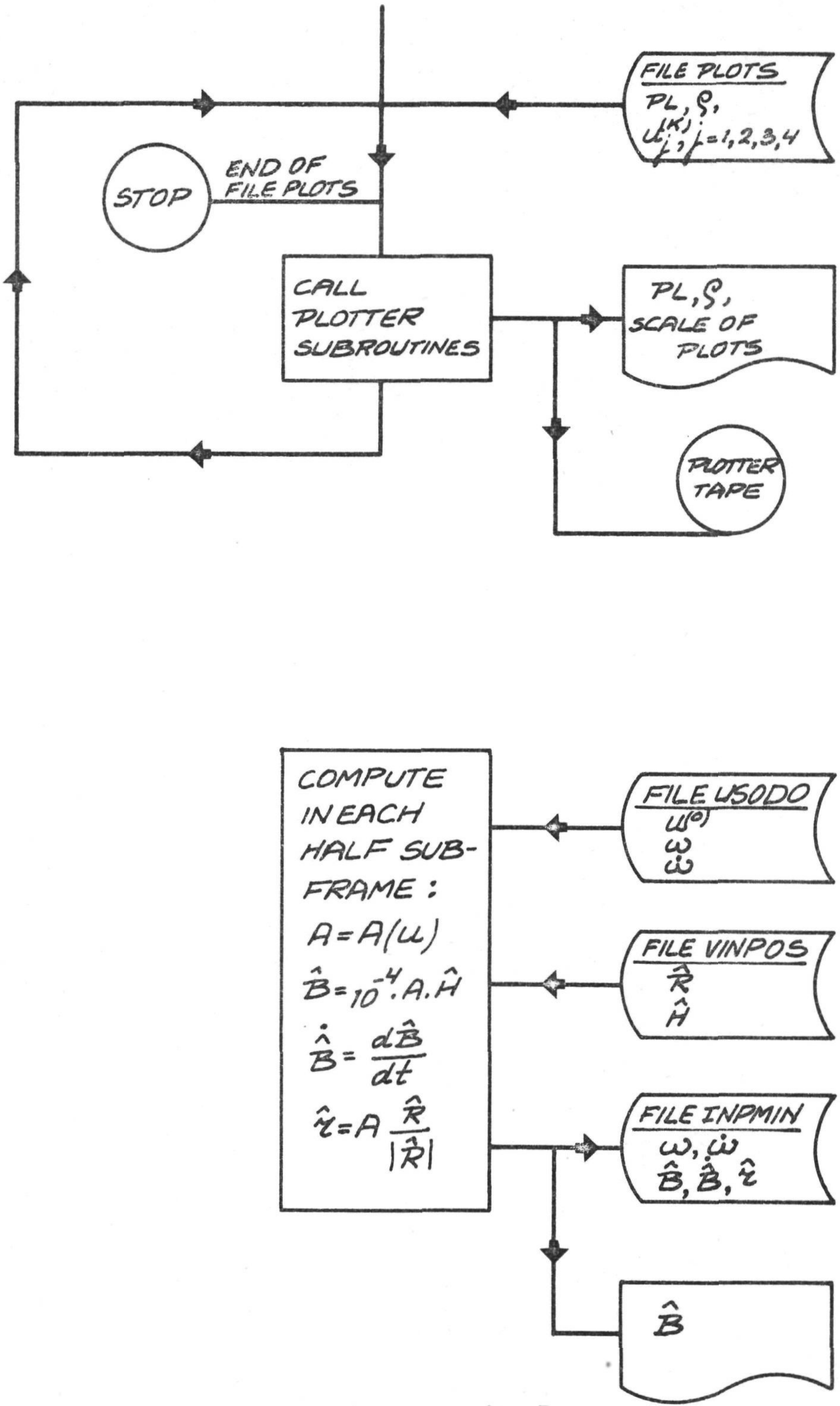

See appendix D

Fig.5 System flow charts of PLOTU and DATACOL

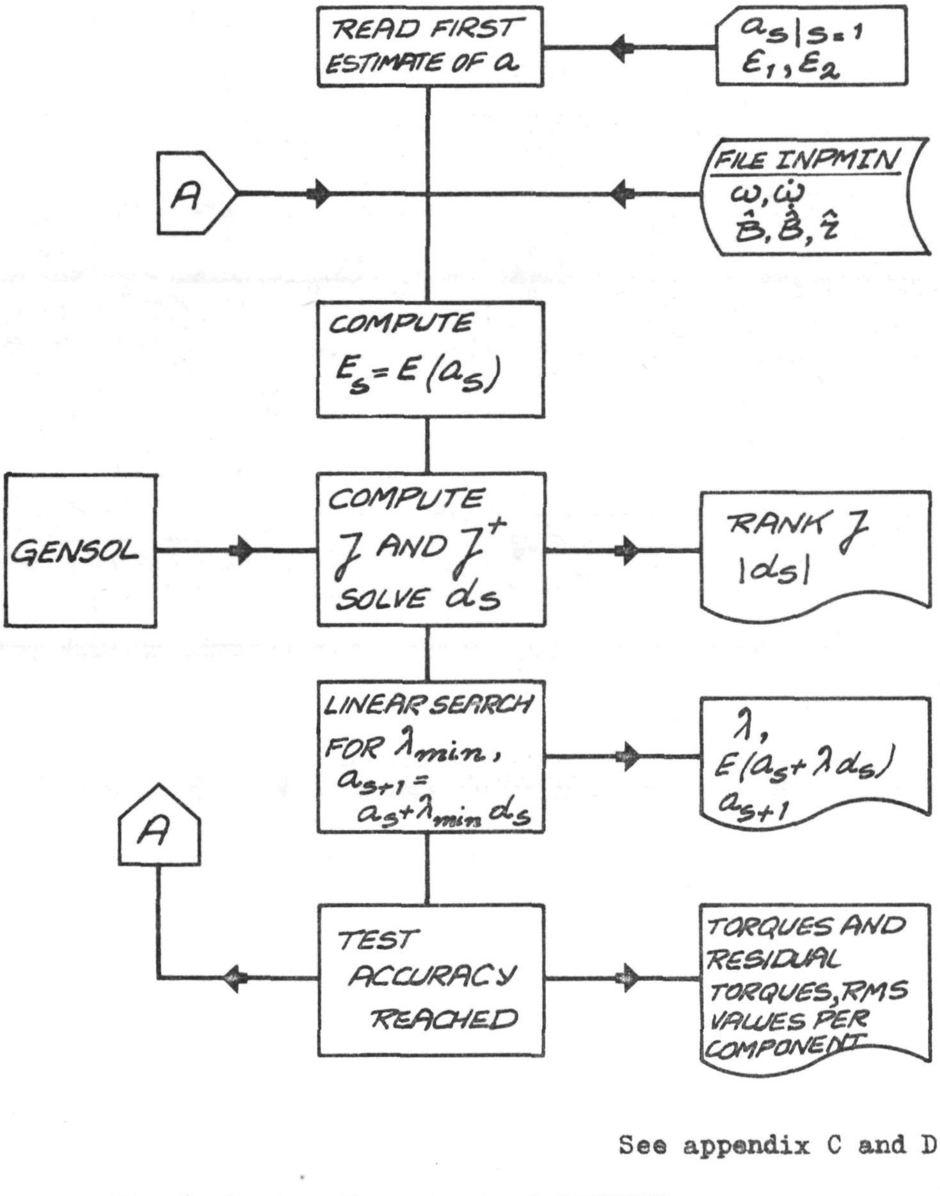

See appendix C and D

Fig.6 System flow chart of FLETMIN

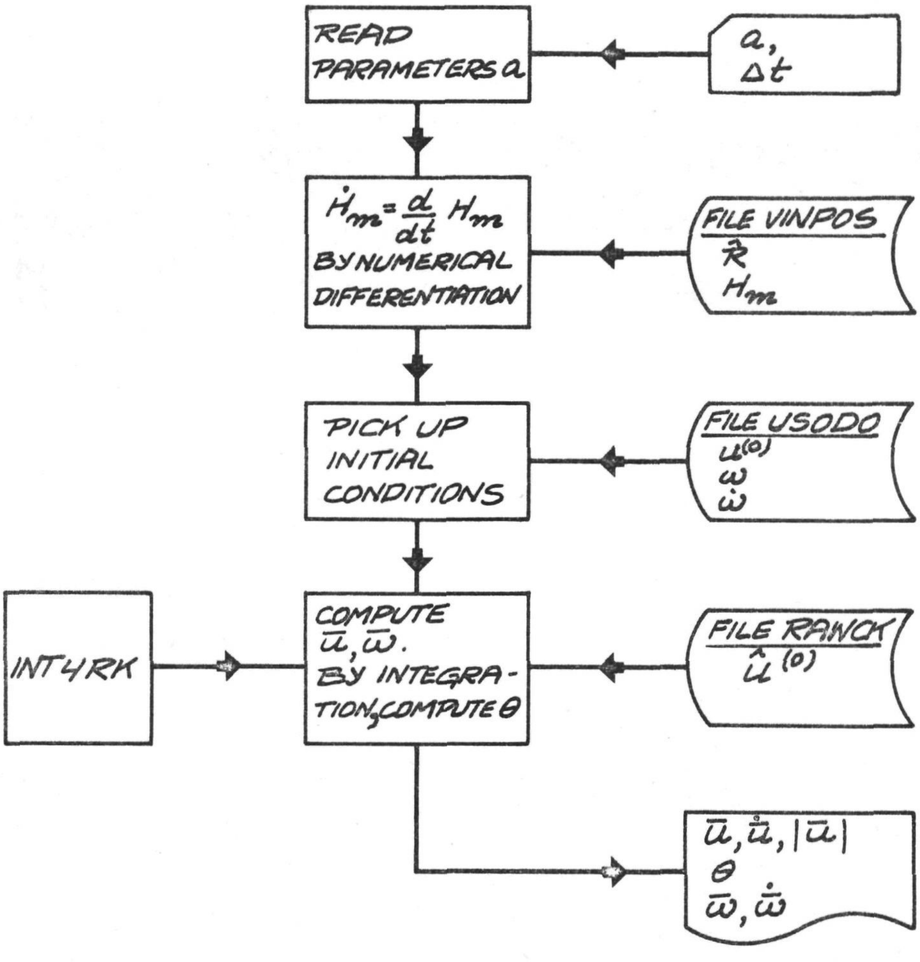

See appendix D and E

Fig.7 System flow chart of EULINT

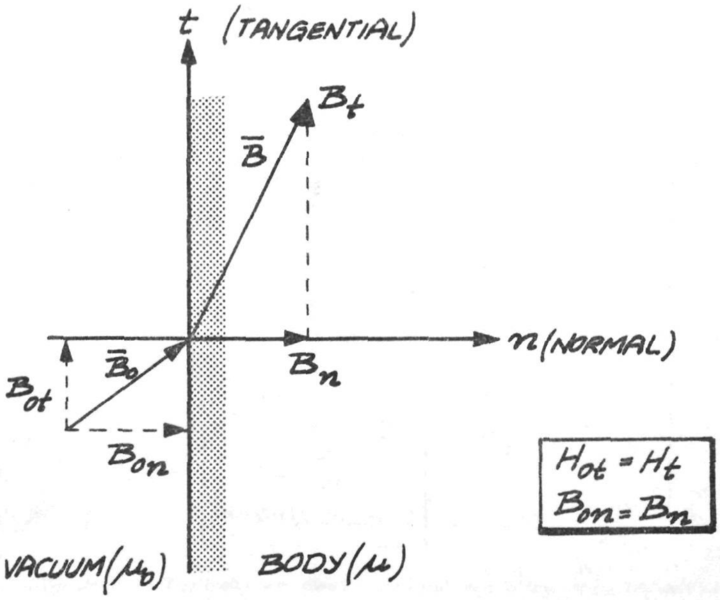

Fig.8 Magnetic boundary conditions

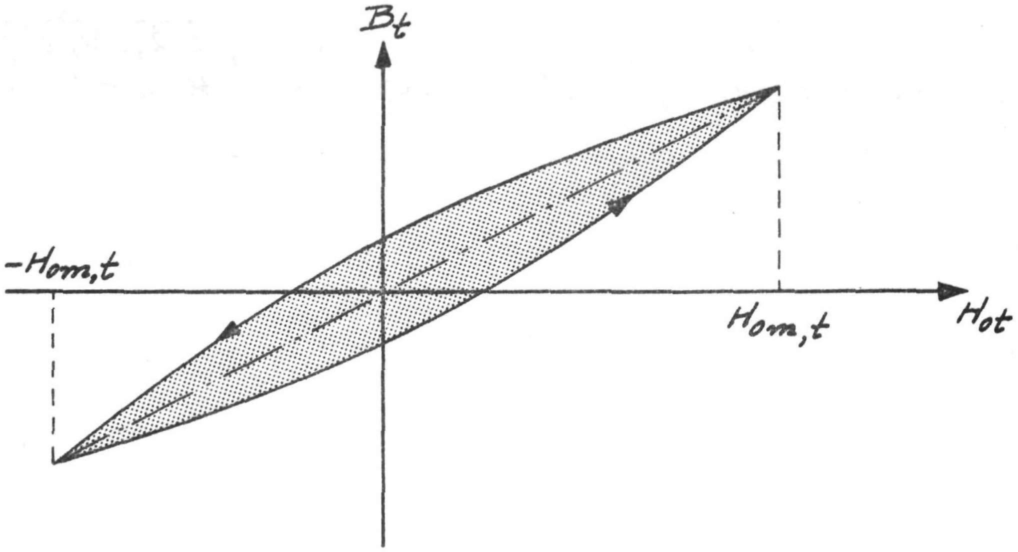

Fig.9 B-H hysteresis curve for symmetric magnetisation (Rayleigh model)

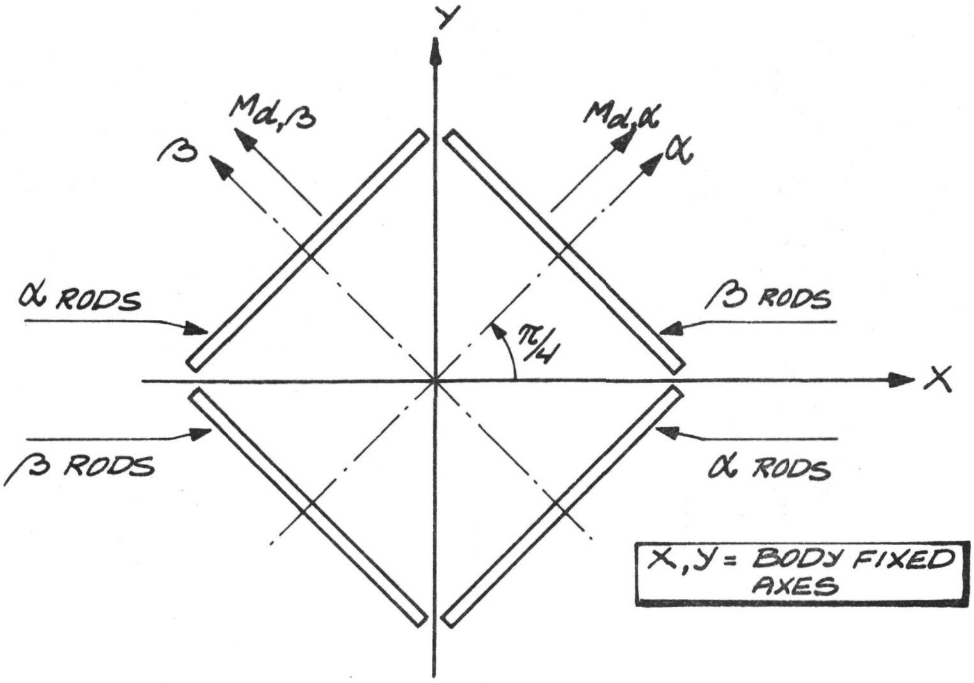

Fig.10 Configuration of hysteresis rods

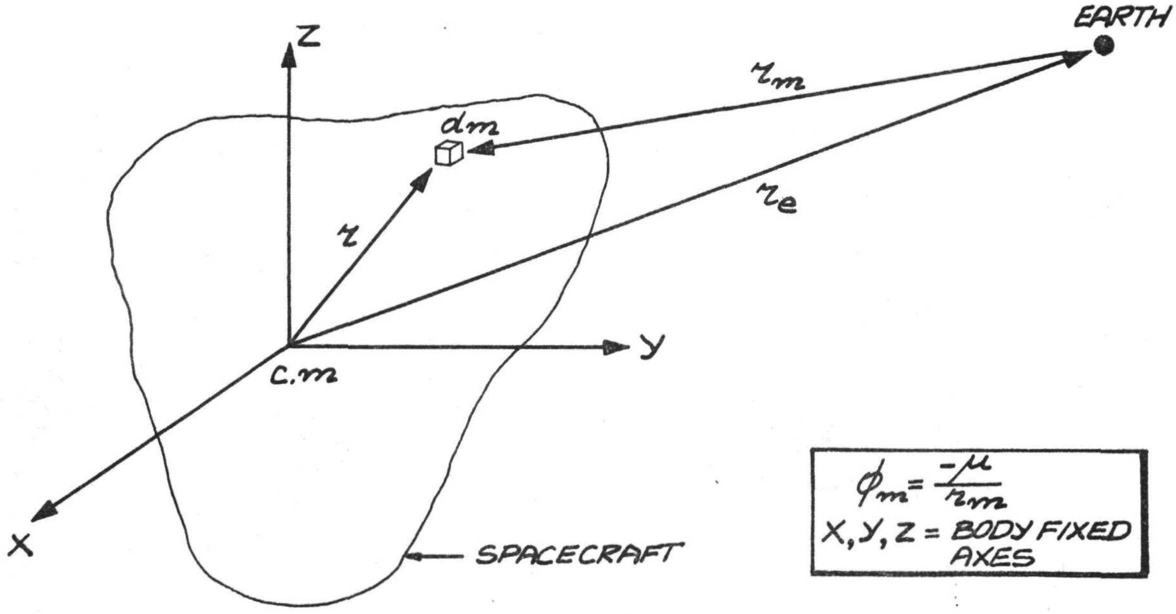

Fig.11 Gravity gradient torque : notation

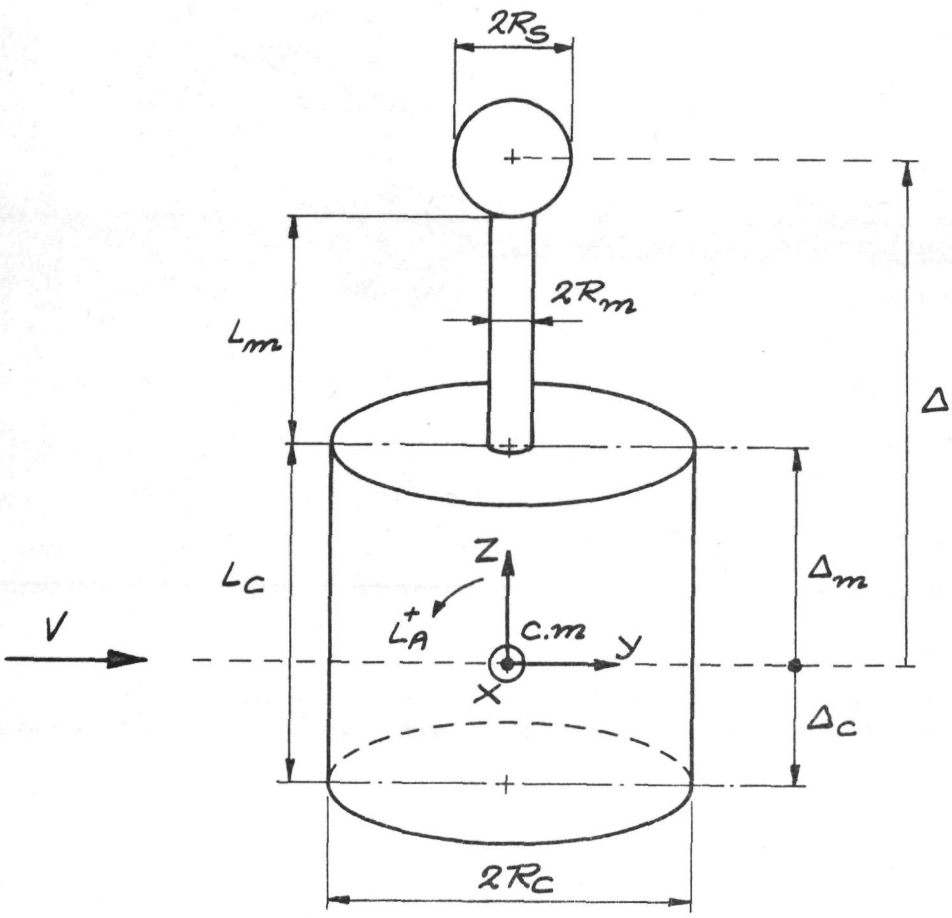

Fig.12 Notations for spacecraft geometry as used in the aerodynamic torque estimate

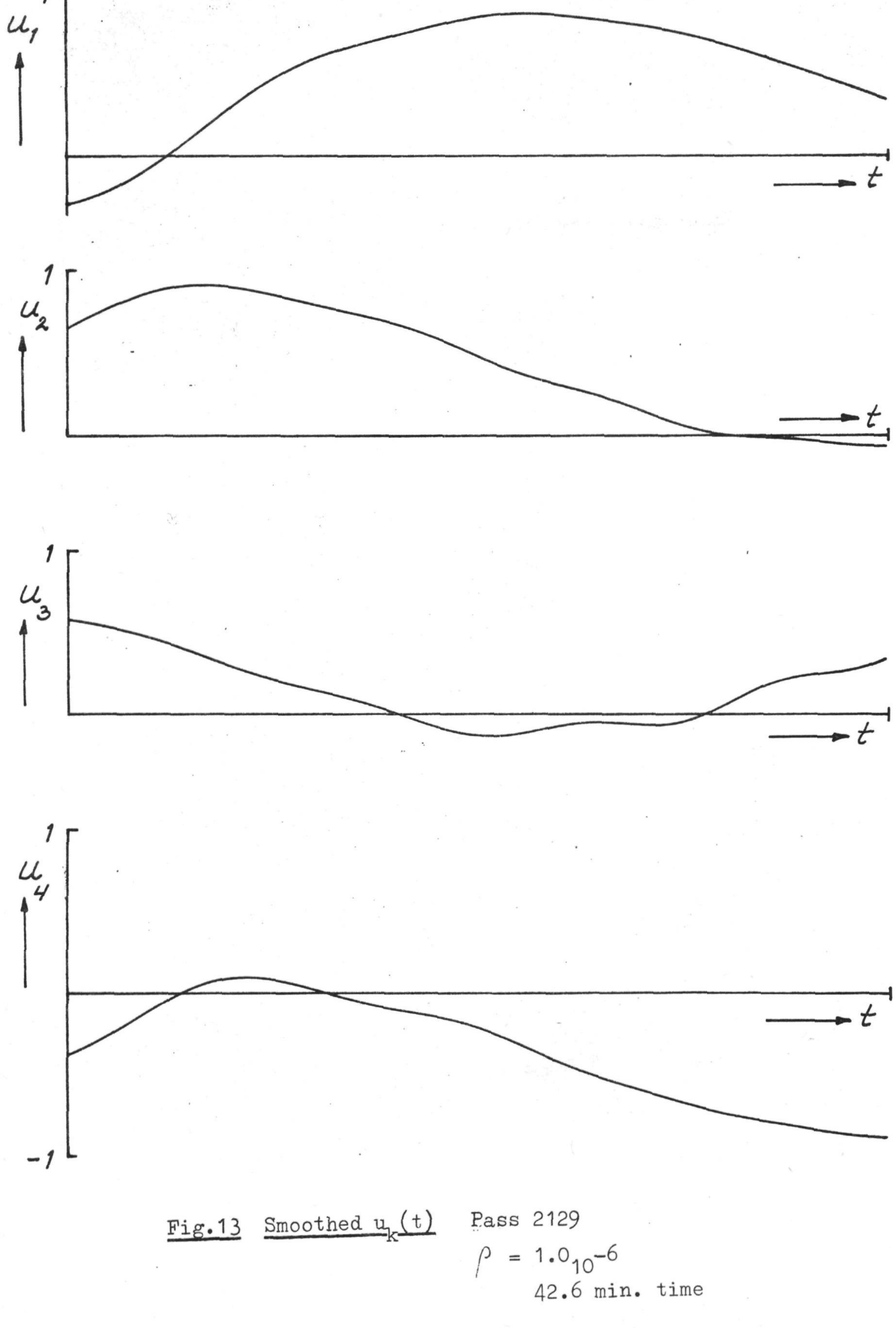

Fig.13 Smoothed $u_k(t)$ Pass 2129

$\rho = 1.0_{10}{-6}$

42.6 min. time

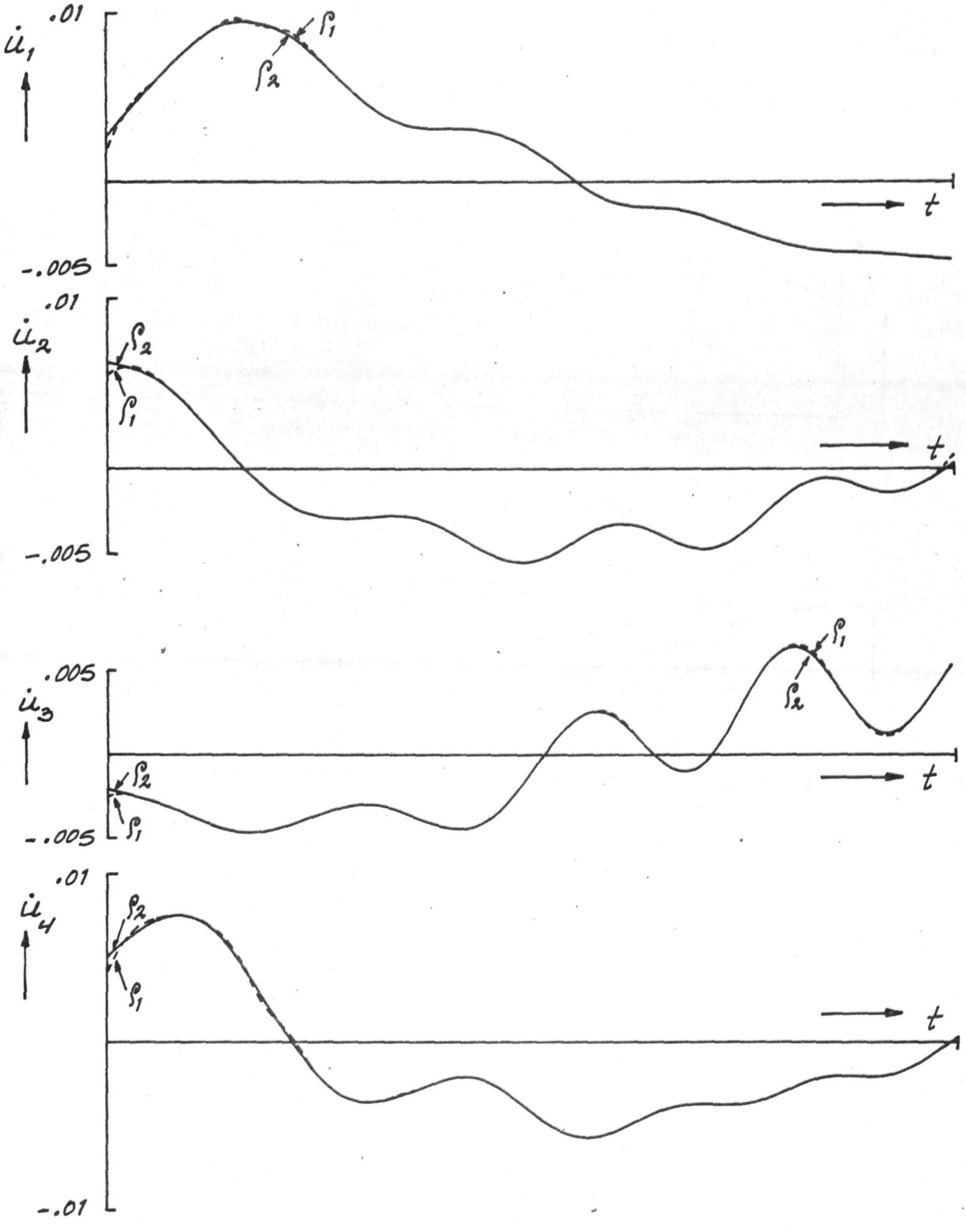

Fig.14 Smoothed $\dot{u}_k(t)$ Pass 2129

$\rho_1 = 4.9_{10}^{-5}$; $\rho_2 = 1.0_{10}^{-6}$

42.6 min. time

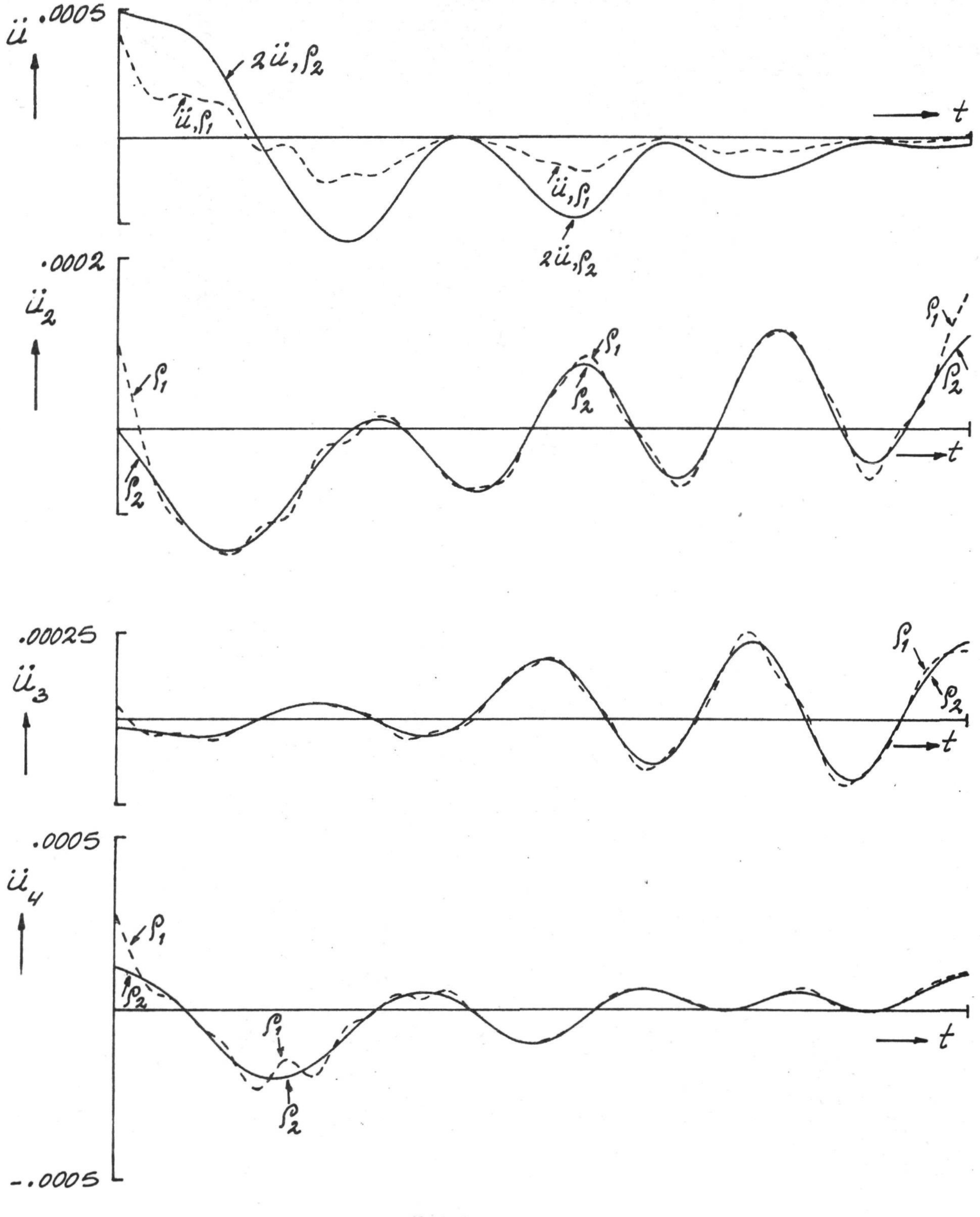

Fig.15 Smoothed $\ddot{u}_k(t)$ Pass 2129

$\rho_1 = 4.9_{10}{}^{-5}$; $\rho_2 = 1.0_{10}{}^{-6}$

42.6 min. time

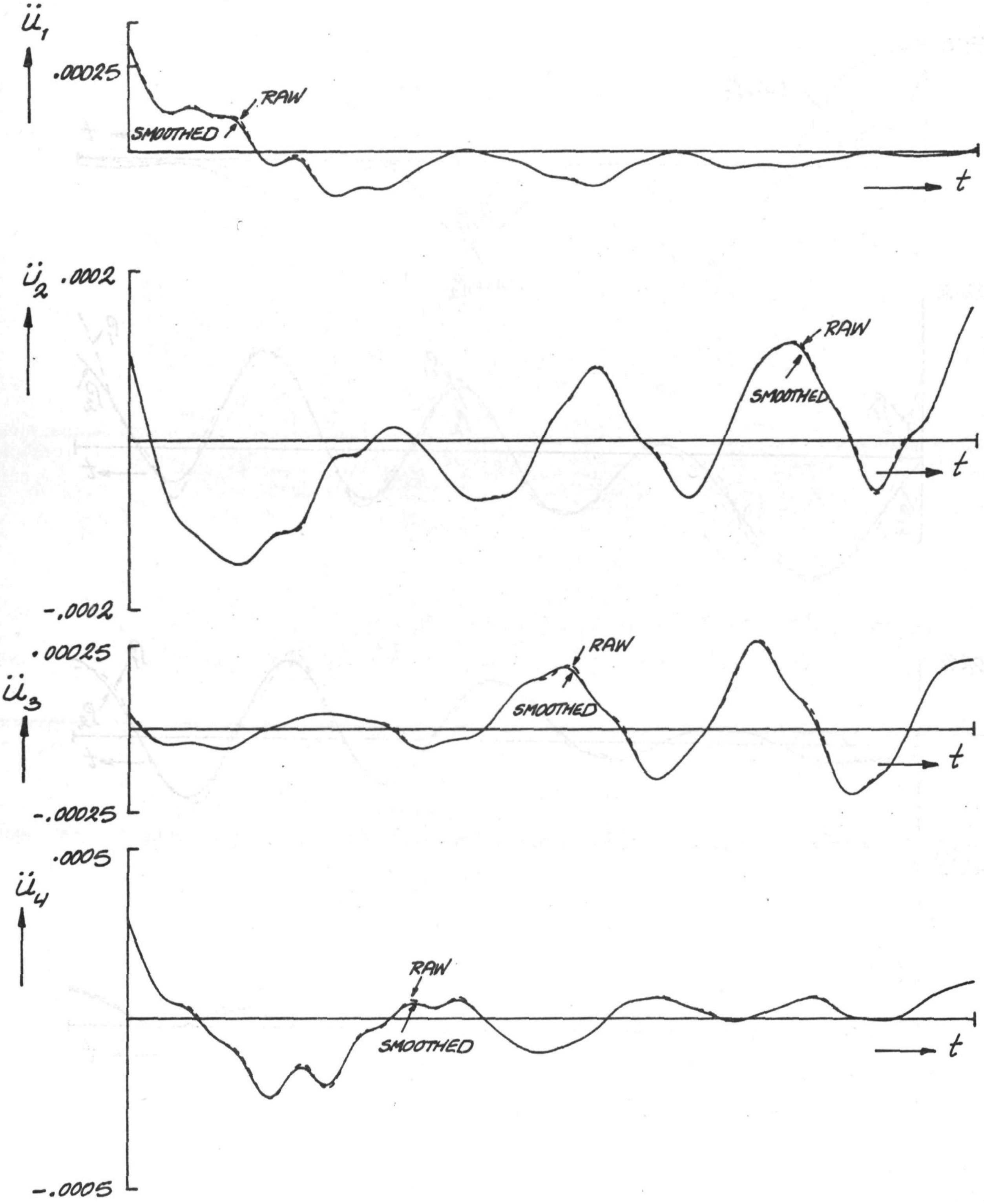

Fig.16 Difference between raw and smoothed $\ddot{u}_k(t)$ Pass 2129

$\rho = 4.9\,{}_{10}{}^{-5}$

42.6 min. time

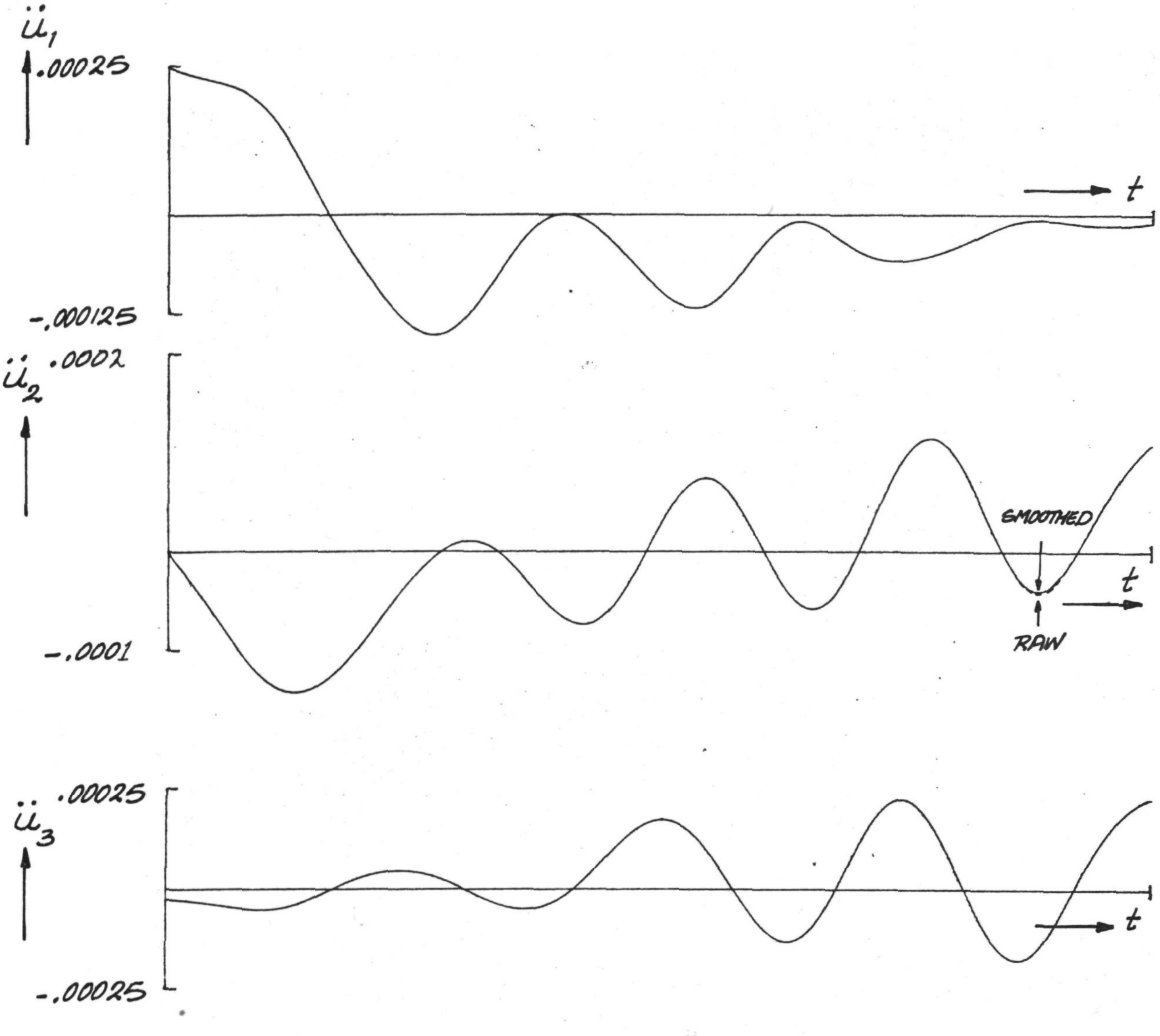

Fig.17 Difference between raw and smoothed $\ddot{u}_k(t)$ (component $\ddot{u}_4$ omitted)

Pass 2129
$\rho = 1.0_{10}-6$
42.6 min. time

Appendix A: SELECTION OF PASSES

A careful selection was made of the telemetered data to be used. The following selection criteria are applied in this particular study:

1. The geomagnetic activity level must be low. This criterion is desirable, as the attitude reconstitution is based on the assumption that the actual geomagnetic field is closely approximated by the model field. A high geomagnetic activity level (geomagnetic storms) would disturb the correspondence, and hence lead to errors in the attitude reconstitution.
   The daily equivalent planetary amplitude Ap may be used as a geomagnetic activity index. If $Ap < 20$ one usually speaks of low activity. Daily values of Ap (Ref. 8) have been plotted versus time in figure 1. Those orbits for which $Ap < 20$ are of interest here.

2. The orbital plane should preferably be roughly normal to the Sun-Earth line, so that large parts of the orbits are illuminated, and the directions of the sun vector and Earth magnetic field lines will not be collinear.
   To obtain the angle between orbital plane and Sun-Earth line as a function of time, a simplified mathematical model was formulated, assuming that the Earth moves with constant angular velocity around the Sun. This model yields the sun vector as a function of time. The direction of the normal to the osculating orbital plane as a function of time may be obtained from the daily values of the osculating elements tabulated in reference 8. One now deduces the time behaviour of the angle Φ between sun vector and orbital plane (Fig. 1, solid line). Note that the error resulting from the assumption of constant Earth angular velocity is roughly nine degrees, leading to an error band of $2 \times 4.5^{\circ}$ width (hatched region in Fig. 1). Those orbits for which $50^{\circ} < \Phi < 90^{\circ}$ (roughly) are of interest.

3. Only altitudes larger than 700 km are to be considered. This criterion insures that the aerodynamic torques (not accounted for in the present attitude model) are small enough to be negligible. (cf. App. G.2)

4. Criteria one and two led to a selection of 130 passes. Criterion three determines the part of those passes that may be used. Subsequently, a data selection program was used to inspect each of these passes with respect to the following three, additional criteria:
   a. the Sun must illuminate more than eighty percent of the pass;
   b. per pass a maximum of five synchronization errors (wrong time flags) is allowed.
   c. the magnetometers were not allowed to operate in the so-called calibration mode.

It was found that of the 130 passes selected on the basis of criteria one, two and three, 22 $^{o}/o$ satisfied criteria 4a, 4b and 4c simultaneously. Results of the application of the latter three criteria are compiled in the following table:

satisfaction of criteria	resulting number of apogee passes	percentage
a	98	75
b	126	97
c	32	25
$a \wedge b$	94	72
$b \wedge c$	32	25
$a \wedge c$	29	22
$a \wedge b \wedge c$	29	22

5. Of the 29 passes satisfying criteria one through four, six had to be rejected as these displayed saturation of the fine magnetometers over rather sizeable parts of the passes. Another pass had to be rejected as it contained an insufficient number of data points.

Thus, satisfaction of criteria four and five occurred for twenty two passes, which is equivalent to a yield of 22/130 = 17 °/o.

6. Two of these acceptable twenty two passes did not contain the fine magnetometer reading (MFY) in each first half-subframe. The missing readings were corrected for by linear interpolation in the readings in the second half-subframes.

In principle it is possible to accept additional passes with a small amount of magnetometer readings in calibration mode, and to correct for this. In this study this possibility was not explored as it was not recognized in time as such.

Appendix B: NUMERICAL DIFFERENTIATION OF QUATERNION PARAMETERS

The quaternion parameters u_k, $k=1(1)4$, in the data points are differentiated twice with respect to time using the smoothing spline function technique outlined in section 3.2. The computation sequence applied to the data of a pass was:

- determine $\dot{u}_k$ from u_k with $q=3$ and $\rho=10^{-6}$;
- " a new $\dot{u}_k$ " $\dot{u}_k$ " $q=2$ " $\rho=1$;
- " $\ddot{u}_k$ " $\dot{u}_k$ " $q=3$ " $\rho=10^{-6}$;
- " a new $\ddot{u}_k$ " $\ddot{u}_k$ " $q=2$ " $\rho=1$.

This computation sequence was taken from ESOC-provided computer programs.

The choice of ρ can be based on Schmidtbauer's analysis of the filtering characteristics of the smoothing spline functions (Ref. 2, App. A) and on the observation that the oscillation periods of the spacecraft are of the order of 6 to 12 minutes. Hence, frequencies above about 0.017 rad/sec may be filtered out of the data. The choice of $\rho=10^{-6}$ corresponds to a cut-off frequency of the smoothing spline function of 0.0156 rad/sec (equivalent to a cut-off period of 6.7 min.).

The differentiation has been carried through with the data points equally spaced at intervals of unit length. This fact has been taken into account when choosing a value of ρ.

It was found that the smoothing with $q=2$ and $\rho=1$ is not effective and might have been deleted from the computation sequence. On the other hand, the data were not affected by this operation.

Appendix C: PARAMETER ESTIMATION WITH PROGRAM FLETMIN

The parameters a_j, j=1(1)5, in the mathematical model are estimated by a method proposed by Fletcher (Ref. 5). Details of the method are presented below.

Equation (12) can be written as

$$E(a) = \sum_{k=1}^{3n} \left\{ f_k(a) \right\}^2 \qquad (C1)$$

where a is the vector of the parameter a_j. The summation is over all squares of the three torque vector components in each data point of a pass.

The parameter vector a minimizing E(a) is computed iteratively. In each iteration step s first a search direction vector d_s is computed from a given parameter vector a_s (see next paragraph). Next, a linear search along the line $a_s + \lambda d_s$ is performed in order to determine the minimum of E(a) on this line:

$$E(a_s + \lambda_{min}\, d_s) = \min_{\lambda \geqslant 0} E(a_s + \lambda d_s) \qquad (C2)$$

The parameter vector vector a_{s+1} for the next iteration step (s+1) is then defined by

$$a_{s+1} = a_s + \lambda_{min}\, d_s \qquad (C3)$$

The search direction vector d_s is determined by minimizing an approximation to E(a) in the neighbourhood of the vector a_s:

$$E_s(d_s) = \sum_{k=1}^{3n} \left[f_k(a_s) + \left(\frac{\partial f}{\partial a}\Big|_{a=a_s} , d_s \right) \right]^2 \qquad (C4)$$

The approximation is non-negative and quadratic in d_s. The expression between square brackets is obtained by approximating $f_k(a)$ near $a=a_s$ by a Taylor series in $d_s=a-a_s$ and truncating after the linear term in the expansion.

The iteration is terminated if:

$$|\lambda_{min}\, d_s| < \varepsilon_1 \quad \text{or} \quad \left[\frac{1}{3n}\left\{E(a_s) - E(a_{s-1})\right\}\right]^{1/2} < \varepsilon_2 \qquad \text{(C5)}$$

where ε_1 and ε_2 are preassigned small constants.

When the mathematical model contains physically meaningless parameters this often results in a poor condition of the minimization problem. In such cases the solution of the least squares problem (C4) poses problems. Difficulties can be avoided, however, by computing d_s with the generalized inverse J^+ of the Jacobian

$$J_{kj} = \frac{\partial f_k}{\partial a_j}\Bigg|_{a=a_s} \qquad \text{(C6)}$$

following Hansen and Lawson (Ref. 6).

The elements of the Jacobian are computed by analytic differentiation, whereas Fletcher follows a procedure equivalent to numerical differentiation. In ill-conditioned minimization problems numerical differentiation should be avoided, however.

Appendix D: DESCRIPTION OF PROGRAM SYSTEM FOR PARAMETER ESTIMATION

For the study a system of six programs was developed. Their function and interrelated use will be sketched in this appendix.

The six programs have the following functions (see also Fig.2):

- ORBDATA : collection of measured data, checking of quality of the data, preliminary data processing, disposition of raw quaternion parameters and other processed measurements to the auxiliary files RAWCK and VINPOS.
- SMODIFF : Smoothing and differentiation of raw quaternion parameters on file RAWCK, disposition of smoothing results to auxiliary files USODO (smoothed parameters) and PLOTS (for plotting purposes).
- PLOTU : Preparation of a magnetic tape for plotting with an off-line plotter.
- COLDATA : Collection of smoothed quaternion parameters and other measured data from files USODO and VINPOS and data processing using smooth quaternion parameters.
- FLETMIN : estimation of parameters a_j, j=1(1)5 in mathematical model (App. C).
- EULINT : integration of equations of motion using given values of the parameters a_j, and comparison of measurements with results obtained by integration (App. E).

Detailed flow charts of each program can be found in figures 3 through 6. These flow charts are useful when details of the programs (available at NLR) have to be studied. A list of symbols accompanying the figures is given on next page.

a	vector of parameters a_j, $j=1(1)5$
$A = A(u)$	rotation matrix, obtained from smoothed u
$\hat{A} = A(\hat{u})$	rotation matrix, obtained from raw u
$\bar{A} = A(\bar{u})$	rotation matrix, obtained by integration of u
$\hat{B} = 10^{-4} A.\hat{H}$	measured magnetic flux vector (body-fixed co-ordinates)
$\dot{\hat{B}} = \frac{d\hat{B}}{dt}$	and numerical first derivative
$\hat{H}$	measured magnetic field strength vector (body-fixed co-ordinates)
H_m $\dot{H}_m = \frac{dH_m}{dt}$	model magnetic field strength vector (inertial co-ordinates) and numerical first derivative
Δt	integration step in time
MMR	magnetometer readings
PL	plot number
$\hat{R}$	measured spacecraft position vector (inertial co-ordinates)
$\hat{r} = A(u) \frac{\hat{R}}{\lvert\hat{R}\rvert}$	unit vector the earths centre (body-fixed co-ordinates)
$\hat{S}$	measured sun vector (body-fixed co-ordinates)
S_m	model sun vector (inertial co-ordinates)
SSR	sun sensor readings
ρ	smoothing parameter
ϑ	error rotation angle (equation (E2))
$\hat{u}$ $\hat{u}^{(o)}$	raw quaternion parameters
u $u^{(o)}$	smoothed quaternion parameters

$u^{(1)}$ $u^{(2)}$	numerical first and second derivative with respect to time of u
$\bar{u}$ $\dot{\bar{u}}$	quaternion parameters and derivatives obtained by integration
$\omega = \omega(u,u^{(1)})$ $u = \dot{\omega}(u,u^{(1)},u^{(2)})$	angular velocity vector and first derivative derived from smoothed $u^{(k)}$
$\bar{\omega}$ $\dot{\bar{\omega}}$	angular velocity vector and first derivative as obtained by integration

Appendix E: THE INTEGRATION OF THE DYNAMICAL EQUATION OF THE SPACECRAFT ATTITUDE MOTION

The results of the parameter estimation can be checked by an integration program. This program is described below.

The equations (1) and (2) and the equations relating the angular velocity components ω_i to the quaternion parameters u_k, k=1(1)4,

$$\begin{bmatrix} \dot{u}_1 \\ \dot{u}_2 \\ \dot{u}_3 \\ \dot{u}_4 \end{bmatrix} = {}^1/_2 \begin{bmatrix} 0 & \omega_1 & \omega_2 & \omega_3 \\ -\omega_1 & 0 & \omega_3 & \omega_2 \\ -\omega_2 & -\omega_3 & 0 & \omega_1 \\ -\omega_3 & -\omega_2 & -\omega_1 & 0 \end{bmatrix} \begin{bmatrix} u_1 \\ u_2 \\ u_3 \\ u_4 \end{bmatrix} \tag{E1}$$

(Ref.1, Eq. (13)) constitute a system of seven first-order, non-linear, ordinary differential equations. They are integrated numerically with the fourth order Runge-Kutta process. The parameters a_j, j=1(1)5 in the Euler equations are given values equal to the least-squares estimates. The unit vectors to the earth center and the earth magnetic field vector (needed in the Euler equations) are computed from the measured positions and times of the spacecraft and from the magnetic field model. Because the measurements are available at time intervals of 6.4 sec., while the Runge-Kutta process requires two points for a complete integration step, the integration step was chosen equal to a multiple of 12.8 sec. The differential equations were integrated forward and backward in time, taking as initial or final values of ω_i, $\dot{\omega}_i$, u_k and $\dot{u}_k$ the smoothed values obtained during parameter optimization.

It was verified that rounding and truncation errors are a few orders of magnitude smaller than the order of magnitude of the computed data.

A suitable error measure is the angular difference between the measured and the numerically integrated attitudes. This difference can be computed using two rotation matrices, A and $\bar{A}$. $\bar{A}$ gives the spacecraft attitude as obtained with numerical integration. A is the attitude computed directly from the measurements. (In both cases a geocentric inertial co-ordinate system is taken as reference system. The rotation matrices $\bar{A}$ and A are related to computed and measured quaternion parameters respectively according to equation (10) of reference 2).

A suitable norm on the angular errors in attitude is the expression

$$2 \cos \vartheta = \mathrm{tr}(A\,\bar{A}^T)-1, \tag{E2}$$

see reference 2, page 22.

Inputs to the computation program are the estimated parameters a_j of a pass, the raw quaternion parameters (computed directly from the measurements) and the spacecraft position in the data points, the integration step, the initial conditions and the data point where the integration has to start. The output consists of computed values of the quaternion parameters and their first derivatives, the angular velocity and acceleration vectors and the error ϑ at the end of each integration step.

A system flow chart of the program is given in figure 7.

Appendix F: MAGNETIC INTERACTION MODEL

An independent derivation of the torques generated by the interaction between the Earth's magnetic field and the spacecraft's permanent magnet and hysteresis rods, leads to results that differ in some respects from the expressions for the torque presented in reference 2. In this appendix, the derivation will be outlined, and the differences with the expressions in reference 2 will be discussed. The results are used in appendix G4 to obtain a numerical estimate of the magnitude of the magnetic torque, which, in turn, leads to a significant conclusion concerning the level of the residual torque.

F.1 Magnetic torque

Consider the torque exerted by a magnetic field in vacuum on a magnetic dipole. An external magnetic field with a magnetic induction B_o (V sec/m^2) exerts on a magnetic dipole moment of strength M_d(Am^2) a torque given by:

$$L_m = M_d \times B_o \qquad \text{Nm} \qquad \text{(F1)}$$

This expression may be found e.g. in references 9 and 10. Care must be exerted in the application of the torque equation, as it differs from those used by a number of authors (e.g. Refs. 11 through 14). Use of rationalized dimensions must also be scrutinously observed.

In the following expressions for the magnetic dipole moment of the permanent magnet and the hysteresis rods will be developed for use in equation (F1).

F.2 Determination of the magnetic dipole moment

If a material body is introduced in the B_o field, one can determine the B field inside the body through application of the proper boundary conditions (Fig. 8) and using the definition of the induced magnetization M and of the magnetic field strength H_o (Ref. 9):

$$B = \mu_o(H_o + M) \mathrel{\hat{=}} \mu H_o \qquad \text{(F2)}$$

where μ_o denotes the permeability of free space and μ the permeability of the body. In general μ depends on H_o.

The boundary conditions $B_n = B_{on}$ and $H_t = H_{ot}$ lead to

$$M_n = 0 \qquad M_t = (\frac{\mu}{\mu_o} - 1)H_{ot} \qquad \text{(F3)}$$

where the indices "n" and "t" denote vector components normal respectively tangential to the body surface.

Inside the body M_n and M_t may differ from their boundary values (F3) at locations interior to the surface. For slender, cylindrical bodies one finds, however, that M_n will differ only slightly from zero. If the body is ferro magnetic, one has typically $\mu/\mu_o \gg 1$, which means that everywhere in the slender, cylindrical body one has in general $M_t/M_n \gg 1$, or, in words: the magnetization vector M is virtually parallel to the cylinder axis everywhere in the body and constant for a given H_o. The magnetic dipole moment M_d of this body follows by integrating (F3) over the volume of the body (rod):

$$M_d = (\frac{\mu}{\mu_o} - 1)\ H_{ot}\ V$$

where V denotes the volume of the rod. This vector is parallel to the axis of the rod. With $\mu/\mu_o \gg 1$ one may therefore approximate the magnetic dipole moment of the rod positioned in an external field of magnetic induction B_o:

$$M_d = \frac{\mu}{\mu_o} H_{ot} V \qquad Am^2 \qquad (F4)$$

where M_d is oriented along the axis of the rod.

F.3 Magnetic dipole moment of the permanent magnet

For permanent magnets positioned in an external magnetic field, one finds, for a certain range of H_{ot} (cf.Ref. 14)

$$B = \mu_o (H_o + M) = \mu_o H_o + \mu_o M_p \qquad (F5)$$

where the index "p" denotes a residual, permanent value of M inside the permanent magnet. The magnitude of this magnetic dipole moment is to be stated by the manufacturer of the magnet. For geomagnetic field strengths, the contribution of H_o to B can be neglected in most applications towards the generation of magnetic torques.

In the ESRO IA application, the nominal magnitude of M_p is 26.6 Am^2 (Ref. 15, table 8.5). The dipole is assumed to make a small angle with the spacecraft z-axis. This assumption leads to the following expression for the components of the dipole moment of the permanent magnet along the spacecraft axes:

$$(M_d)_{p.m.} = \begin{pmatrix} M_{d,x} \\ M_{d,y} \\ M_{d,z} \end{pmatrix}_{p.m.} = - M_p \begin{pmatrix} a_3 \\ a_4 \\ 1 \end{pmatrix} \qquad A.m^2 \qquad (F6)$$

where a_3 and a_4 denote the small misalignment angles of the permanent magnet with respect to the spacecraft z axis (Ref. 2, Fig. 4.2) and where "p.m." stands for permanent magnet.

F.4 Magnetic dipole moment of the hysteresis rods

The dependence of the magnetic dipole moment of hysteresis rods on the external magnetic field is usually given in the form of a so-called B-H curve, which relates the B_t field in a rod to the component H_{ot} of the external H_o field, that is tangential to the rod (Fig. 8). In order to use information from these curves, substitute equation (F2) into (F4) to obtain

$$M_d = \frac{V}{\mu_o} \cdot B_t\,(H_{ot}) \qquad \text{(F7)}$$

Following the approach of Schmidtbauer (Ref. 2) the (symmetric) Rayleigh model is used to analytically relate B_t to H_{ot} (Fig. 9 and Ref. 12). Upon deletion of the index "t" for the sake of clarity, one has the Rayleigh relation

$$B = (\mu_a + 2\vartheta . H_{om})\, H_o - \vartheta\, (H_{om}{}^2 - H_o{}^2)\ \mathrm{sign}\,(\dot{H}_o) \qquad \text{(F8)}$$

which is quadratic in nature. A method to determine the numerical values of the constants is discussed in appendix G 4. In numerical applications one must verify that the material is indeed far from saturated; otherwise the Rayleigh model will not be applicable. Also, symmetric oscillatory motion around the x and y axes is assumed.

Substitution of (F8) in (F7) yields the following expression for the magnetic dipole moment of a hysteresis rod:

$$M_d = b_1 H_o - b_2\, (H_{om}^2 - H_o^2)\ \mathrm{sign}\,(\dot{H}_o) \qquad \mathrm{Am}^2 \qquad \text{(F9)}$$

where

$$\left.\begin{aligned} b_1 &\triangleq \frac{V}{\mu_o}\,(\mu_a + 2\vartheta H_{om}) && \mathrm{m}^3 \\ b_2 &\triangleq \frac{V}{\mu_o} . \vartheta && \frac{\mathrm{m}^4}{\mathrm{A}} \end{aligned}\right. \qquad \text{(F10)}$$

This result for a rod will now be applied to the ESRO IA spacecraft. In this spacecraft, four sets of five rods each are oriented at angles of $\pi/4$ radians with respect to the spacecraft x and y axes (Fig. 10).*

Let the external magnetic field strength have the components H_{ox} and H_{oy} along the x and y axes respectively. It then follows that the components along the α and β axes of the rod frame (Fig. 10) are

$$H_{o,\alpha} = (H_{o,x} + H_{o,y})/\sqrt{2}\ ; \quad H_{o,\beta} = (-H_{o,x} + H_{o,y})/\sqrt{2} \qquad \text{(F11)}$$

The magnetic dipole moment induced in the α- and β-rods now follows from (F9):

$$\begin{aligned} M_{d,\alpha} &= b_1\, H_{o,\alpha} - b_2\, (H^2_{om,\alpha} - H^2_{o,\alpha})\ \text{sign}\ (\dot{H}_{o,\alpha}) \\ M_{d,\beta} &= b_1\, H_{o,\beta} - b_2\, (H^2_{om,\beta} - H^2_{o,\beta})\ \text{sign}\ (\dot{H}_{o,\beta}) \end{aligned} \qquad \text{(F12)}$$

Decomposition of this moment along the x and y axes yields:

$$M_{d,x} = (M_{d,\alpha} - M_{d,\beta})/\sqrt{2} \quad \text{Am}^2; \quad M_{d,y} = (M_{d,\alpha} + M_{d,\beta})/\sqrt{2} \quad \text{Am}^2 \qquad \text{(F13)}$$

whereas $M_{d,z} = 0$.

---

* Reference 7 (page 4) states that the rods are parallel to the x and y axes. Schmidtbauer bases his model on this particular configuration. On the other hand, reference 15 states that the rods are rotated in the x-y plane over an angle of $\pi/4$ radians (Figs 4.4 and 4.17, p. 181, p. 185, Fig. 8.10, Fig. 9.6 and Fig. 14.5). The analysis of the present appendix is based on the latter configuration.

This resulting system is now analyzed for more insight and to yield expressions suitable for numerical evaluation. Consideration of the expression for the magnetic moment of the hysteresis rods shows a linear part (associated with b_1) and a nonlinear part (associated with b_2).

Taking the linear part first:

$$(M_{d,\alpha})_{lin} = b_1 \, H_{o,\alpha} = \frac{b_1}{\sqrt{2}} \, (H_{o,x} + H_{o,y})$$

$$(M_{d,\beta})_{lin} = b_1 \, H_{o,\beta} = \frac{b_1}{\sqrt{2}} \, (-H_{o,x} + H_{o,y})$$

and hence, in vector form:

$$(M_d)_{lin} = b_1 \, (H_{o,x}, H_{o,y}, 0) \quad \text{in the x,y,z reference system} \qquad \text{(F14)}$$

These terms generate a torque (equation (F1)):

$$(L_d)_{lin} = (M_d)_{lin} \times B_o = \frac{b_1 \, B_{o,z}}{\mu_o} \begin{pmatrix} B_{o,y} \\ -B_{o,x} \\ 0 \end{pmatrix}$$

However, one can show that precisely the same torque is generated by a hypothetical linear dipole moment

$$(M_d)_{lin} = - \frac{b_1}{\mu_o} \, (0,0,B_{o,z}) \qquad \text{(F15)}$$

which is of the same form as the one presented in reference 2. Introducing the definition of b_1 and noting that $B_{o,z} \cong - |B_o|$, one has

$$(M_d)_{lin} = \frac{V(\mu_a + 2\vartheta H_{om})}{\mu_o^2} \, (0,0, |B_o|) \qquad \text{(F16)}$$

where again, H_{om} is the maximum of the component of the external magnetic field strength parallel to the rod.

It will now be established whether this linear part may be contracted with the contribution of the permanent magnet, as done in reference 2. The particular contraction is valid if the following inequality condition is satisfied:

$$|M_d|_{\text{lin}} \ll |M_d|_{\text{p.m.}} \tag{F17}$$

Using numerical values obtained in appendix G.4:

$|M_d|_{\text{p.m.}} = 26.6 \quad \text{Am}^2$

$\mu_a = 5 \times 10^{-3} \quad \text{Vsec/Am}$

$V = 1.55 \times 10^{-5} \quad \text{m}^3$

$\vartheta = 4.54 \times 10^{-4} \quad \text{Vsec/A}^2$

$\mu_o = 4\pi/10^7 \quad \text{Vsec/Am}$

$H_{om} = 4.17 \quad \text{A/m}$

$|B_o| = 3 \times 10^{-5} \quad \text{Vsec/m}^2$

leads to $|M_d|_{\text{lin}} = 2.58 \text{ Am}^2$

The value 2.58 Am^2 is certainly not very small compared to 26.6 Am^2, and hence the inequality (F17) is considered to hold to an insufficient degree.

Yet another important observation follows from the numerical evaluation of equation (F16). According to appendix G 4 one has $H_{om} = \varepsilon_m \dfrac{|B_o|}{\mu_o}$. Clearly, H_{om} depends on the maximum angular excursion ε_m of the spacecraft z-axis away from the magnetic field lines. Therefore, in equation (F10) :

$$b_1 = \frac{V}{\mu_o}\left(\mu_a + 2\vartheta H_{om}\right) = \frac{V}{\mu_o}\left(\mu_a + 2\,\vartheta\,\frac{|B_o|}{\mu_o}\cdot\varepsilon_m\right) \qquad \text{m}^3 \tag{F18}$$

where ε_m denotes the most <u>recent</u> value of the maximum angular excursion. Substituting the above numerical values yields

$$b_1 = \frac{V}{\mu_o} (5 + 21.7\ \varepsilon_m) \times 10^{-3} \quad m^3 \quad (\varepsilon_m \text{ in radians}).$$

One then finds that the second term equals the first term for $\varepsilon_m = 0.23$ rad. = 13.2 degrees. In actual flight, the maximum angle ε_m may range from a few degrees to about 20 degrees (Ref. 16). It then follows that treating b_1 as a constant leads to errors of the same order of magnitude as b_1 (i.e. of 100 °/o). Moreover, the term B_o occurring in the vector part of equation (F16) and in b_1 may vary in the order of 100 °/o, as B_o varies with altitude as well as with geocentric latitude. For example, in the latter case one finds that for the same altitude, the value of B_o at the magnetic poles is twice the value at the magnetic equator. Thus, treating B_o as a constant leads to equally unacceptable errors.

Summarizing these observations:

1. the linear part of the hysteresis dipole moment (b_1) should not be contracted with the dipole moment of the permanent magnet.
2. in the linear part of the hysteresis dipole moment, neither b_1 nor B_o should be treated as constants. The dipole is to be used in the form

$$(M_d)_{lin} = \frac{V}{\mu_o^2} \left(\mu_a + \frac{2\vartheta |B_o|}{\mu_o} \cdot \varepsilon_m\right) (0, 0, |B_o|) \qquad \text{(F19)}$$

   where B_o and the maximum excursion angle ε_m vary with time and where $V.\mu_a/\mu_o{}^2$ and $2V\vartheta/\mu_o{}^3$ are true constants (which may be determined as new, a priori unknown parameters).
3. the above analysis should be made separately for the rods in the α-direction and for those in the β-direction (Fig. 10).

Next, the nonlinear part is treated. Assuming that the spacecraft oscillates sinusoidally with respect to the magnetic field lines, and with negligible damping, the following relations can be derived (cf. Ref. 2):

$$H_{o,\alpha} = H_{om,\alpha} \sin\omega t \Longrightarrow H_{om,\alpha}^{\;2} - H_{o,\alpha}^{\;2} = \left(\frac{\dot{H}_{o,\alpha}}{\omega_o}\right)^2 ,$$

$$\text{where } \omega_o^{\;2} = \frac{\left\{M_p - (M_{d,z})_{lin}\right\} |B_o|}{I_{av}}$$

where I_{av} denotes the average moment of inertia for an axis in the spacecraft x,y plane.

Thus:

$$(M_{d,\alpha})_{n.l.} = - b_2 \dot{H}_{o,\alpha} \; |\dot{H}_{o,\alpha}| \; /\omega_o^{\;2}$$

$$(M_{d,\beta})_{n.l.} = - b_2 \dot{H}_{o,\beta} \; |\dot{H}_{o,\beta}| \; /\omega_o^{\;2}$$

where the index "n.l." stands for non-linear.

Upon substitution of the expressions for $\omega_o^{\;2}$ and for $H_{o,\alpha}$ and $H_{o,\beta}$.

$$(M_{d,\alpha})_{n.l.} = -a_5 \, (\dot{B}_{o,x} + \dot{B}_{o,y}) \; |\dot{B}_{o,x} + \dot{B}_{o,y}| \; / \; |B_o|$$

$$(M_{d,\beta})_{n.l.} = -a_5 \, (-\dot{B}_{o,x} + \dot{B}_{o,y}) \; |-\dot{B}_{o,x} + \dot{B}_{o,y}| \; / \; |B_o| \qquad \text{(F20)}$$

where

$$a_5 \triangleq \frac{b_2}{2\mu_o^{\;2}} \cdot \frac{I_{av}}{M_p - (M_{d,z})_{lin}} \qquad \text{(F21)}$$

which is constant if $(M_{d,z})_{lin}$ is treated as a constant.

Note that this definition of a_5 differs from the one used in reference 2.

The expressions (F20) are now substituted in (F13) to yield the dipole moment due to the non-linearity in the hysteresis rods.

F.5 Summary

The magnetic dipole moment due to the permanent magnet is given by equation (F6). This equation agrees with the corresponding result in reference 2.

The magnetic dipole moment due to the hysteresis rods has been derived on the assumption that the α and β axes of the rods are rotated with respect to the x and y axes of the spacecraft over an angle of $\pi/4$ radians. The linear part of the dipole moment is given by equation (19), and the non-linear part is given by equations (F13) and (F20). These equations differ from those presented in reference 2. Numerical estimates are developed in appendix G 4.

Appendix G: ESTIMATES OF SPACECRAFT TORQUES

This appendix contains order of magnitude estimates of the following types of torque:

1. gravity gradient torque;
2. aerodynamic torque;
3. solar radiation torque;
4. magnetic torque.

G.1 Estimate of the gravity gradient torque

The gravity gradient torque on a body of arbitrary shape is defined as

$$L_G = -\int r \times (\nabla\Phi_m)\, dm \tag{G1}$$

where dm denotes an infinitesimal quantity of spacecraft mass, r defines the position of dm with respect to body fixed reference axes with origin at the center of mass of the spacecraft; Φ_m denotes the potential of the Earth's gravitational field at dm; and the integration is carried out over all spacecraft mass. Note that the torque vector L_G is identical to the vector L_{M3} used in the main body of the report.

Following and extending the analysis of reference 17 and using the notation shown in figure 11, one finds that equation (G1) may be written in the scalar form:

$$L_{G,x} = 3\frac{\mu}{r_e^3}\left[\left(\frac{x}{r}\ \frac{z}{r}\right)_e \cdot I_{xy} - \left(\frac{x}{r}\frac{y}{r}\right)_e \cdot I_{xz} + \left(\frac{z^2}{r^2} - \frac{y^2}{r^2}\right)_e I_{yz} + \left(\frac{y}{r}\cdot\frac{z}{r}\right)_e (I_{zz}-I_{yy})\right]$$

$$L_{G,y} = 3\frac{\mu}{r_e^3}\left[-\left(\frac{y}{r}\ \frac{z}{r}\right)_e I_{xy} + \left(\frac{x^2}{r^2} - \frac{z^2}{r^2}\right)_e I_{xz} + \left(\frac{x}{r}\ \frac{y}{r}\right)_e I_{yz} + \left(\frac{x}{r}\ \frac{z}{r}\right)_e (I_{xx} - I_{zz})\right]$$

$$L_{G,z} = 3\frac{\mu}{r_e^3}\left[\left(\frac{y^2}{r^2} - \frac{x^2}{r^2}\right)_e I_{xy} + \left(\frac{y}{r}\ \frac{z}{r}\right)_e I_{xz} - \left(\frac{x}{r}\ \frac{z}{r}\right)_e I_{yz} + \left(\frac{x}{r}\ \frac{y}{r}\right)_e (I_{yy} - I_{xx})\right]$$

$$\tag{G2}$$

These expressions reduce to those presented in reference 17 for the special case where the body fixed reference axes x,y,z are chosen to coincide with the spacecraft principal axes of inertia. Note that the quantities $(\ldots)_e$ are measured with respect to the body fixed reference axes.

In the case of the ESRO IA Spacecraft one assumes $I_{xz} = I_{yz} = 0$. Furthermore, the principal axes of inertia ξ, η, ζ are assumed to be obtainable from the x,y,z axes by a simple rotation around the z-axis over an angle a_2. This leads to the following results (Ref. 2):

$$\begin{aligned} I_{xx} &= I_\zeta + (I_\eta - I_\xi)\sin^2 a_2; & I_{xy} &= (I_\eta - I_\xi)\sin a_2 . \cos a_2; \\ I_{yy} &= I_\eta - (I_\eta - I_\xi)\sin^2 a_2; & I_{xz} &= 0; \\ I_{zz} &= I_\zeta; & I_{yz} &= 0; \end{aligned} \qquad \text{(G3)}$$

where: $I_\xi = 8.07 \text{ kgm}^2$

$I_\eta = 9.32 \text{ kgm}^2$

$I_\zeta = 5.53 \text{ kgm}^2$

Using the typical value (Section 4) $a_2 = 0.45$ rad. one finds, correct to two decimal places:

$$\begin{aligned} I_{xx} &= 8.31 \text{ kgm}^2 & I_{xy} &= 0.49 \text{ kgm}^2 \\ I_{yy} &= 9.08 \text{ kgm}^2 & I_{xz} &= 0 \quad \text{kgm}^2 \\ I_{zz} &= 5.53 \text{ kgm}^2 & I_{yz} &= 0 \quad \text{kgm}^2 \end{aligned} \qquad \text{(G4)}$$

Furthermore, for a small eccentricity orbit one may approximate the factor μ/r_e^3 by μ/a^3, where a denotes the semi major axis. For an apogee at 1400 km altitude and a perigee at 260 km one finds:

$$\frac{\mu}{r_e^3} = 1.064 \times 10^{-6} \text{ sec}^{-2} \qquad \text{(G5)}$$

The worst case magnitude of the torques defined in equation (G2) can now be evaluated:

$$|L_{G,x}| \leqslant 3 \times (1.064 \times 10^{-6}) \left[\frac{1}{2} \times 0.49 + 0 + 0 + \frac{1}{2} \times 3.55 \right] = 6.45 \times 10^{-6} \text{ Nm} = 64.5 \text{ dyne cm}$$

$$|L_{G,y}| \leqslant 3 \times (1.064 \times 10^{-6}) \left[\frac{1}{2} \times 0.49 + 0 + 0 + \frac{1}{2} \times 2.78 \right] = 5.22 \times 10^{-6} \text{ Nm} = 52.2 \text{ dyne cm}$$

$$|L_{G,z}| \leqslant 3 \times (1.064 \times 10^{-6}) \left[1 \times 0.49 + 0 + 0 + \frac{1}{2} \times 1.26 \right] = 3.58 \times 10^{-6} \text{ Nm} = 35.8 \text{ dyne cm}$$

(G6)

G.2 Estimate of the aerodynamic torque

The aerodynamic torque exerted on the spacecraft is defined as

$$L_A = \int r \times (p + \tau)\, dA \qquad \text{(G7)}$$

where r defines the vectorial position of the elementary surface area dA with respect to the spacecraft center of mass, and p and τ denote the vectorial pressure and shear stress resp., exerted on dA by the interaction between spacecraft and surrounding atmosphere.

The interaction between spacecraft and surrounding atmosphere takes place in the free molecular flow regime. Different models exist for the calculation of pressure and shear stress exerted on an elementary surface area dA moving in the free molecular flow regime. Different models do lead to different results and considerable care must therefore be exerted in the interpretation of these results.

An estimate of the order of magnitude of the aerodynamic torque is developed on the basis of a recently proposed aerodynamic interaction model (Ref. 18). This estimate involves both atmospheric density and velocity in the form (ρ V^2). This quantity will be evaluated at the lower altitude of the apogee passes; i.e. at 700 km altitude.

The velocity is obtained from the energy equation:

$$V^2 = \mu \left(\frac{2}{r} - \frac{1}{a}\right) \tag{G8}$$

For an apogee at 1400 km altitude*) and a perigee at 260 km altitude, one finds for the semi major axis $a = 7.108 \times 10^6$ m. For an altitude of 700 km one finds for the radial distance: $r = 7.078 \times 10^6$ m. Substitution in equation (G8) then yields: $V^2 = 5.655 \times 10^7$ (m/sec)^2.

Care must be exerted in finding "the density" at 700 km altitude. The density at that altitude depends strongly on the level of solar activity and on the local time. The numerical estimate will use weighted average values.

Recall that the spacecraft was launched in October 1968. During its first half year in orbit the solar activity was represented by an average flux of about $F = 175 \times 10^{-22}$ W/m^{2}Hz. of the solar radiation at a wavelength of 10.7 cm (cf. Ref. 8 and Fig. 1 of Ref. 19). Superimposed on thisaverage value are fluctuations of about 50×10^{-22} W/m^2 Hz at most; cf. figure 1. Neglecting these fluctuations, F will be taken to be 175×10^{-22} W/m^2 Hz. This value corresponds to Model Six of the ten CIRA 1965 atmospheres (Ref. 20). Model Six shows that the density ρ at 700 km altitude varies from 3.363×10^{-14} kg/m^3 at four hours local time to 3.380×10^{-13} kg/m^3 at fourteen hours local time. These values suggest that $\rho = 3 \times 10^{-13}$ kg/m^3 is a useful upper value for the torque estimate.

The above considerations result in:

$$(\rho V^2)_{700\ \mathrm{km}} = 1.696 \times 10^{-5}\ \mathrm{N/m^2}.$$

---

*) Note that the apogee altitude has decreased from its initial value of 1535 km, due to the influence of the atmosphere. Perigee altitude remains almost constant during this early phase of orbit decay.

A refined estimate of the aerodynamic torque may be obtained by using the detailed aerodynamic interaction model developed and discussed in reference 18. Specifically, this model will be used to calculate the torque due to interaction with an incident flow directed along the spacecraft y-axis (Fig. 12), as this situation would result in the largest value for the aerodynamic torque for a given value of ρV^2.

The central body consists of an "effective" cylinder, replacing the actual central cylinder and truncated cones. Using data from reference 7, one finds:

central body : $L_c \cong 0.84$ m
$R_c = 0.38$ m
central mast : $L_m \cong 0.55$ m
$R_m = 0.0125$ m
sphere : $R_s = 0.05$ m

Also, reference 7 assumes the location of the center of gravity at about 0.43 m below the top plate on the z-axis. Thus, one deduces:

$\Delta_m = 0.38$ m
$\Delta_c = 0.46$ m
$\Delta_s = 0.98$ m

The torque contributions are (Ref. 18, with $\alpha = 0$):

for the central body: $L_{A,c} = (\rho V^2) \;\; L_c \, R_c \, (L_c - 2.\Delta_c)(\frac{2}{3} b_1 + b_3 - \frac{\pi}{4} b_2)$

$$= (\rho V^2)(\frac{2}{3} b_1 + b_3 - \frac{\pi}{4} b_2).(2.55 \times 10^{-2})$$

for the central mast: $L_{A,m} = (\rho V^2) \quad L_m R_m (L_m + 2.\Delta_m)(\frac{2}{3} b_1 + b_3 - \frac{\pi}{4} b_2)$

$$= (\rho V^2)(\frac{2}{3} b_1 + b_3 - \frac{\pi}{4} b_2)(9 \times 10^{-3})$$

for the sphere $\quad : L_{A,s} = (\rho V^2) \quad \pi R_s^2 \, \Delta_s \quad (\frac{1}{2} b_1 - \frac{2}{3} b_2 + b_3)$

$$= (\rho V^2)(\frac{1}{2} b_1 - \frac{2}{3} b_2 + b_3)(7.7 \times 10^{-3})$$

where the appropriate dimensions have been substituted.

To evaluate b_1, b_2 and b_3, the following values are assumed:

$$\sigma_N = \frac{1}{2} , \sigma_T = \frac{1}{2}, \sigma_a = \frac{3}{4}, \gamma = \frac{5}{3} , \frac{T_\omega}{T_i} = \frac{273 \ ^oK}{1200 \ ^oK}$$

and the molecular speed ratio S is roughly 8. This leads to:

$$b_1 = -1 \qquad b_2 = 0.164 \qquad b_3 = - \frac{1}{2}$$

Substituting these values in the expressions for the component torques and summing, yields:

$$|L_A| = |L_{A,c} + L_{A,m} + L_{A,s}| = (1.28 \times 10^{-2}) \ \rho V^2 \quad Nm \qquad (G9)$$

and hence

$$|L_A|_{700} = 2.18 \times 10^{-7} \ Nm = 2.18 \ dyne \ cm \qquad (G10)$$

G.3 Estimate of the radiation torque

Radiation incident on the surface of a spacecraft leads to a torque of the form (G7). The generation of p and τ is mainly due to solar radiation, Earth-reflected sunlight, and infrared emission from the Earth and the Earth atmosphere. The latter two sources lead to varying torque contributions as the spacecraft moves along its orbit (Ref. 21, Fig. 6). For an order of magnitude estimate it will be assumed that the total radiation input is equal to one and a half times the solar radiation input.

Little is known about the precise interaction between incoming radiation and spacecraft surface. However, for an order of magnitude estimate one might assume adsorption followed by completely diffusion re-emission. This case leads to the following expressions for pressure and shear stress (Refs. 21 and 22):

$$P = \frac{I}{c} \cdot (\sin\alpha + \frac{2}{3}) \sin\alpha$$
$$\tau = \frac{I}{c} \cdot \sin\alpha \cos\alpha \qquad \text{(G11)}$$

where I denotes the radiation input, c the speed of light, and α the acute angle between the surface element under consideration and the direction to the radiation source.

Substitution of (G11) in (G7) and integration leads to the total torque exerted on the spacecraft by radiation. Instead of carrying out the analysis in detail, it is instructive to compare (G11) with the corresponding expressions for the pressure and shear stress exerted on the spacecraft by aerodynamic interaction.(equations (3.3) and (3.4) of Ref. 18). The following correspondences can then be established:

$$\rho V^2 \Longleftrightarrow I/c \quad ; \quad \sigma_T \Longleftrightarrow 1$$
$$(2 - \sigma_N) \Longleftrightarrow 1 \quad ; \quad \frac{\sigma_N}{2S} \sqrt{\frac{\pi T_r}{T_i}} \Longleftrightarrow \frac{2}{3} \qquad \text{(G12)}$$

leading to

$$b_1 = 0 \qquad b_2 = \frac{2}{3} \qquad b_3 = -1 \qquad \text{(G13)}$$

Thus, the radiation torque may readily be obtained by repeating the analysis of appendix G 2 (aerodynamic torque), using these correspondences.

Reference 22 gives for the solar radiation input: $I = 1400\ W/m^2$. The total radiation input therefore equals $I = 2100\ W/m^2$. With $c = 3 \times 10^8$ m/sec one has $I/c = 7 \times 10^{-6}\ N/m^2$.

Substitution of this value in the place of ρV^2, and of the values for b_1, b_2 and b_3, in the expressions for the torque contribution by central body, central mast, and sphere, and subsequent summation of these component torques, yields the following estimate for the total radiation torque:

$$|L_{RAD}| \leqslant 10^{-7}\ N.m = 1 \text{ dyne cm} \qquad (G14)$$

G.4 Estimate of the magnetic torque

Following appendix F, the torque exerted on the spacecraft due to the interaction between the Earth's magnetic field and the permanent magnet and hysteresis rods, is given by:

$$L_M = M_d \times B_o \ (Nm) \qquad (G15)$$

where the contribution to M_d from the permanent magnet is given by equation (F6), and from the hysteresis rods by equations (F19) and (F20).

To estimate the magnitude of the total magnetic torque, a number of preliminary assumptions and calculations are made:

1. The magnitude of the external magnetic induction is taken equal to the latitudinally averaged value at an average altitude during an apogee pass. The average altitude during an apogee pass is equal to 1050 km. The value of B_o at this altitude varies between 2×10^{-5} and 4×10^{-5} Vsec/m^2 as function of latitude. The assumed average value is therefore $B_o = 3 \times 10^{-5}$ V/sec/m^2.

2. The dipole moment of the permanent magnet is assumed to have the nominal value: 26.6 Am^2 (Ref. 15).
3. The orientation of the permanent magnet is assumed to be nominal; i.e., parallel to the spacecraft z-axis: $a_3 = a_4 = 0$.
4. The spacecraft z-axis oscillates with respect to the local magnetic field vector. The maximum value ε_m of the oscillating angle between the z-axis and the field vector is taken to be ten degrees (cf. Ref. 16).
5. The numerical values of the hysteresis parameters b_1 and b_2 defined in appendix F are derived from data presented in reference 15.

From assumptions 1 and 4 one can calculate the maximum value of the component of the Earth magnetic field strength in the rod-plane:

$$H_{om,\alpha\beta} = H_{om} = \varepsilon_m \frac{B_o}{\mu_o} = 4.17 \frac{A}{m}$$

This value lies far below the saturation value (cf. Ref. 7) and therefore justifies use of the Rayleigh model for the hysteresis rods (as far as the saturation criterion is concerned).

The determination of the numerical values for b_1 and b_2 may be based on the determination of μ_a and ϑ (cf. app. F) from various figures shown in reference 15. Several approaches are possible. The most reliable approach was found to involve measurements of the linear part of the Rayleigh curves shown in figure 8.5 of reference 15. According to appendix F, the hysteresis curves may be modelled by the equation

$$B = (\mu_a + 2\vartheta H_{om})\, H_o - \vartheta\, (H_{om}{}^2 - H_o{}^2)\ \mathrm{sign}\ (\dot{H}_o) \qquad \text{(G16)}$$

where μ_a and ϑ are the same for all curves. If the values of H_o and B at the two extremes of the curves are taken from several curves, and substituted in equation (G16), one obtains an overdetermined system of linear equations in the two unknown parameters μ_a and ϑ;

each equation being of the form

$$\mu_a + \vartheta \cdot (2H_{om}) = B_m/H_{om} \tag{G17}$$

Using measurements of the two extremes of three curves, the following approximate result was obtained:

$$\mu_a = 5 \times 10^{-3} \ \frac{\mathrm{Vsec}}{\mathrm{Am}} \qquad \vartheta = 4.54 \times 10^{-4} \ \frac{\mathrm{Vsec}}{\mathrm{A}^2} \tag{G18}$$

with an error of the order of two percent.
Finally, note that the rod volume in either α or β direction is equal to $V = 1.55 \times 10^{-5}\ \mathrm{m}^3$ (Ref. 15, table 8.6).
One can now derive the numerical values for b_1 and b_2, defined by equation (F10):

$$b_1 = 1.08 \times 10^{-1}\ \mathrm{m}^3 \qquad b_2 = 5.6 \times 10^{-3}\ \frac{\mathrm{m}^4}{\mathrm{A}} \tag{G19}$$

The maximum induced magnetic induction in the rods is calculated for the case of oscillations around the rods' β axis. At this maximum the nonlinear contribution (b_2) vanishes, and the magnetic dipole moment may therefore be calculated from the linear part as given by equation (F16) or F19):

$$(M_d)_{rods} = (0,\ 0,\ 2.58) \quad \mathrm{Am}^2 \tag{G20}$$

Using assumptions 2 and 3 together with equation (F6) one finds for the magnetic dipole moment of the permanent magnet:

$$(M_d)_{p.m.} = (0,\ 0,\ -26.6) \quad \mathrm{Am}^2 \tag{G21}$$

The total dipole moment is given by their sum:

$$M_d = (M_d)_{p.m.} + (M_d)_{rods} = (0,\ 0,\ -24.02) \quad \mathrm{Am}^2 \tag{G22}$$

The resulting total torque is calculated from equation (G15):

$$\begin{pmatrix} L_{M,x} \\ L_{M,y} \\ L_{M,z} \end{pmatrix} = \begin{pmatrix} M_{d,y} B_{o,z} & - & M_{d,z} B_{o,y} \\ M_{d,z} B_{o,x} & - & M_{d,x} B_{o,z} \\ M_{d,x} B_{o,y} & - & M_{d,y} B_{o,x} \end{pmatrix} \qquad (G23)$$

where $|B_{o,z}| = 3 \times 10^{-5}$ Vsec/m^2 and

$$|B_{o,x}| = |B_{o,y}| = \frac{\mu_o}{\sqrt{2}} H_{om\,\alpha\beta} = 3.7 \times 10^{-6} \text{ Vsec/m}^2$$

(the square root arises due to the oscillation around the β-axis) Substitution of these values and those of expression (G22) in the torque equation yields the estimates

$$|L_{M,x}| \text{ and } |L_{M,y}| \leq 8.9 \times 10^{-5} \text{ Nm} = 890 \text{ dyne cm} \qquad (G24)$$

$$|L_{M,z}| = 0$$

Recall that this result was obtained at the upper limit $|H_{o\alpha\beta}| \rightarrow H_{om\alpha\beta}$, which led to the vanishing of the nonlinear part of the dipole moment induced in the rods. An estimate for the torque due to this nonlinear part may be obtained from equations (F12) and (F13) by setting $H_{o\alpha} = 0$ together with $H_{o\beta} = 0$, $H_{om\beta} = 0$ (oscillations around the β axis). Thus:

$$(M_{d\alpha}, M_{d\beta})_{rods} = (-b_2 H^2_{om,\alpha} \text{ sign } (\dot{H}_{o,\alpha}), 0)$$

$$= (\pm 9.7 \times 10^{-2}, 0) \quad \text{Am}^2$$

and hence expressed, in x,y,z co-ordinates:

$$(M_d)_{rods} = (\pm 6.9 \times 10^{-2}, \pm 6.9 \times 10^{-2}, 0) \text{ Am}^2 \qquad (G25)$$

Substitution in the torque equation (G23) yields the estimate for the torque due to the nonlinear (hysteresis) part:

$$\begin{aligned} &|L_{M,x}| \text{ and } |L_{M,y}| \leqslant 2.07 \times 10^{-6}\ \text{Nm} = 20.7\ \text{dyne cm} \\ &|L_{M,z}| = 0 \end{aligned} \qquad \text{(G26)}$$

Notice that an erroneous mathematical model for the nonlinear hysteresis part would lead to an error of about twenty dyne cm, which constitutes a sizeable part of the present level of residual torque. One is tempted to conclude that inclusion of the present hysteresis model as developed in appendix F might reduce the observed residual torque considerably.

Appendix H EXAMPLES OF SMOOTHING DIFFERENTIATION AND RESULTS OF NUMERICAL INTEGRATION

Numerical experiments, carried out with the smoothing spline function algorithm in order to check the choice of the weighting parameter ρ (section 3.2, equation (9)) and to investigate the possible occurrence of end effects in the smoothed results, indicate that the value of ρ used in the computations ($\rho = 10^{-6}$) is reasonable, but that end effects are present. The last conclusion is also supported by the results obtained with integration. Evidence for these conclusions is presented in this appendix.

The choice of ρ was checked by applying the smoothing differentiation algorithm to the quaternion parameters obtained from measured data of pass 2129. The total number of data points for each parameter was 400, corresponding to a time interval of 42.6 min (Fig. 13). The computation sequence applied was:

- determine $\dot{u}_k$ from u_k with $q = 3$
- determine $\ddot{u}_k$ from $\dot{u}_k$ with $q = 3$, $k = 1(1)4$, ρ fixed;
- smooth $\ddot{u}_k$ to a new $\ddot{u}_k$ with $q = 3$

where q is the order of the derivative in equation (7). This sequence was applied with five different values of ρ:

ρ	cut-off period
4.9×10^{-5}	3.5
1.1×10^{-5}	4.5
3.3×10^{-6}	5.5
1.2×10^{-6}	6.5
10^{-6}	6.7

The cut-off periods were computed according to the analysis of Schmidtbauer (Ref. 2, appendix A); oscillations with periods less than the cut-off period are heavily smoothed by the algorithm, those with larger periods not.

The changes in computed results with varying ρ are systematic. It is therefore sufficient to inspect only results for $\rho = 4.9 \times 10^{-5}$ and 10^{-6}.

The results for u_k (Fig. 13) are virtually identical, those for $\dot{u}_k$ (Fig. 14) differ somewhat (in particular at the ends), and those for $\ddot{u}_k$ (Fig. 15) are different for the two values of ρ. Smoothing of raw $\ddot{u}_k$-values has effect (Fig. 16) but does not lead to physically acceptable values when $\rho = 4.9_{10}-5$. On the other hand, smoothing of the raw $\ddot{u}_k$-values for $\rho = {}_{10}-6$ has practically no effect (Fig. 17), and the period of the oscillations in $\ddot{u}_k$ (42.6 : 4 $\cong$ 10 minutes) is thus sufficiently large compared to the cut-off period of 6.7 minutes. This justifies the choice of $\rho = {}_{10}-6$ in the computations (see App. B).

The occurrence of end effects is visible in figures 14 and 15. In order to analyze these effects one may note from equation (10) that near the end point $t = t_o$ for $t > t_o$ the smoothing of the quaternion parameters u_k implies that the smoothed values satisfy relations of the form:

$$
\begin{array}{rcl}
\dddot{u}_k & = & O\,(t-t_o)^3 \\
\ddot{u}_k & = & 2c_k + O\,(t-t_o)^4 \\
\dot{u}_k & = & b_k + 2c_k(t-t_o) + O\,(t-t_o)^5 \\
u_k & = & a_k + b_k\,(t-t_o) + c_k\,(t-t_o)^2 + O\,(t-t_o)^6
\end{array}
$$

where a_k, b_k and c_k are constants. If the raw u_k-data do not exhibit this behaviour and are smoothed heavily, we may expect that near the end point $t=t_o$ the smoothed u_k will have an approximately more linear first and constant second derivative than the non-smooth data. Comparison of the results for $\rho = 4.9_{10}-6$ and $\rho = {}_{10}-6$ in figures 14 and 15 shows these effects. The same conclusion is valid for the other end point $t=t_n$.

The integration program was run for pass 2129, taking initial and final data and estimates of the parameters a_j computed with $\rho = 10^{-6}$ (App. E). The results are:

- forward integration from 1st to 400th data point: max $|\vartheta| = 31.9^\circ$,
- backward integration from 400th to 1st data point: max $|\vartheta| = 6.4^\circ$,
- backward integration from 400th to 60th data point: max $|\vartheta| = 3.2^\circ$,
- forward integration from 60th to 400th data point: max $|\vartheta| = 12.2^\circ$,

where ϑ is the error angle introduced in appendix E. It is evident that end effects at the beginning of the pass can account for the error decreases that result if the first sixty data points are not considered during integration.

Appendix I AERODYNAMIC PARAMETER ESTIMATION

For succesful estimation of aerodynamic parameters (Ref. 23, section 2B) it is necessary that the aerodynamic torque be large on the average, compared to the residual torque. In this appendix an estimate will be made of the magnitude of the aerodynamic torque in the perigee region, and of the total time available for the acceptance of significant telemetered attitude data.

An estimate of the magnitude of the aerodynamic torque at any altitude can be deduced from equation (G9):

$$|L_A| = (1.28 \times 10^{-2})\ (\rho V^2) \quad \mathrm{Nm} \tag{I1}$$

Perigee is located at an altitude of 260 km. Using equation (G8) one finds for the velocity at perigee: $V^2 = 6.402 \times 10^7\ (\mathrm{m/sec})^2$.

Density at perigee is determined using the same arguments as in appendix G 2 . Model Six of the CIRA 1965 atmosphere shows that the density ρ at 260 km varies from $5.174 \times 10^{-11}\ \mathrm{kg/m^3}$ at six hours local time to $8.522 \times 10^{-11}\ \mathrm{kg/m^3}$ at sixteen hours local time. These values suggest that $\rho = 7 \times 10^{-11}\ \mathrm{kg/m^3}$ is a useful value for the torque estimate.

The above considerations result in:

$$(\rho V^2)_{260\ \mathrm{km}} = 4.481 \times 10^{-3}\ \mathrm{N/m^2}$$

and hence

$$|L_A|_{260} \leqslant 5.736 \times 10^{-5}\ \mathrm{Nm} = 573.6\ \mathrm{dyne\ cm} \tag{I2}$$

This value is an estimate for the upper bound of the aerodynamic torque. Clearly, as altitude increases, both density and velocity decrease, leading to a decrease in the magnitude of the aerodynamic

torque. For example, consider the case of flight at an altitude of 500 km.
Using equation (G8), one finds for the velocity at 500 km altitude: $V^2 = 5.983 \times 10^7\ (\mathrm{m/sec})^2$. Model Six of the CIRA 1965 atmosphere shows that the density ρ at 500 km varies from $5.782 \times 10^{-13}\ \mathrm{kg/m^3}$ at four hours local time to $2.766 \times 10^{-12}\ \mathrm{kg/m^3}$ at fourteen hours local time. These values suggest that the average value $\rho = 1.672 \times 10^{-12}\ \mathrm{kg/m^3}$ is a useful value for the torque estimate. These considerations result in:

$$(\rho V^2)_{500\ \mathrm{km}} = 10^{-4}\ \mathrm{N/m^2}$$

and hence:

$$|L_A|_{500} \leqslant 1.28 \times 10^{-6}\ \mathrm{Nm} = 12.8\ \text{dyne cm} \qquad (I3)$$

Finally, the time to move from 500 km altitude down to perigee and again up to 500 km altitude is calculated.

For an apogee at 1400 km altitude and a perigee at 260 km altitude one finds for the semi major axis: $a = 7.108 \times 10^6\mathrm{m}$, and for the eccentricity: $e = 0.0791$. Using the conic equation one then finds that an altitude of 500 km corresponds to a true anomaly of 70.67 degrees, and hence to an eccentric anomaly of 65.85 degrees. Finally, using Kepler's time equation one finds that the arc from perigee to an altitude of 500 km is traversed in 17.04 min. Thus, the total time from 500 km down to perigee and again up to 500 km is equal to 34.08 min.

Summarizing, the aerodynamic torque at perigee has been estimated to be about 573 dyne cm or smaller, and the aerodynamic torque at 500 km has been estimated to be about 12.8 dyne cm or smaller. Assuming a residual torque of about 20 dyne cm, one finds for the "signal-to-noise" ratio at perigee: $S/N \leqslant 28.7$, and at 500 km: $S/N \leqslant 0.64$. One concludes that the trajectory arc below 500 km would be quite suitable for estimation of aerodynamic parameters as outlined in reference 23. The passage time of 34.08 min is large enough to be acceptable.